

# Controls on the distribution of hydrous defects in forsterite from a thermodynamic model

Joshua M R Muir<sup>\*1,4</sup>, Michael Jollands<sup>3</sup>, Feiwu Zhang<sup>1</sup>, Andrew M. Walker<sup>2,4</sup>

Corresponding author: Joshua M R Muir [j.m.r.muir@mail.gyig.ac.cn](mailto:j.m.r.muir@mail.gyig.ac.cn)

1) State Key Laboratory of Ore Deposit Geochemistry, Institute of Geochemistry, Chinese Academy of Sciences, 99 West Lincheng Road, Guiyang, Guizhou 550081, China

2) Department of Earth Sciences, University of Oxford, South Parks Road, Oxford OX1 3AN, United Kingdom

3) Lamont-Doherty Earth Observatory, 61 Rt 9W, Palisades, NY 10964, USA

4) Department of Earth Sciences, University of Leeds, Leeds, LS2 9JT, UK

## ORCIDs

J. M. R. Muir: 0000-0002-0879-4373, M. Jollands: 0000-0003-1442-5133, F. Zhang: 0000-0002-4979-0790, A. M. Walker: 0000-0003-3121-3255

Words:9336

## Abstract

The distribution of hydrogen across different crystallographic sites and point defects in forsterite determines how many properties, such as rheology, conductivity and diffusion are affected by water. In this study, we use lattice dynamics and Density Functional Theory (DFT) to build a thermodynamic model of H-bearing defects in Al,Ti bearing forsterite. From this, the distribution of hydrogen in forsterite as a function of pressure (P), temperature (T), water, Al and Ti concentration is determined. Primarily, hydrogen

distribution in forsterite is complex and highly varied in different P, T and composition regimes. Therefore, extrapolation of properties that depend upon water between these different regimes is non-trivial. This extrapolation has often been done by determining exponents which describe how defect-specific defect concentrations or properties dependant upon them vary with water concentration/fugacity. We show here that these exponents can vary radically across common experimental and geophysical P, T and  $[\text{H}_2\text{O}]_{\text{bulk}}$  ranges as the favoured hydrogen-bearing defects change. In general, at low pressures hydrogen favours Mg vacancies (high temperatures) or complexes with titanium (low temperatures) whilst at high pressures, hydrogen favours Si vacancies regardless of all other conditions. Higher values of  $[\text{H}_2\text{O}]_{\text{bulk}}$  also favours hydrated Si vacancies. We evaluate these distributions along geotherms and find that hydrogen distribution and thus its effect on forsterite properties is highly varied across the expected conditions of the upper mantle and thus cannot be simply represented. No such distribution of hydrogen has been previously constructed and it is essential to consider this hydrogen distribution when considering the properties of a wet mantle.

Keywords: Forsterite; Hydrogen; Water; Point Defects; Titanium; Aluminium; DFT

## 1 Introduction

Olivine,  $(\text{Mg,Fe})_2\text{SiO}_4$ , is a nominally anhydrous mineral (NAM), but may contain trace amounts of  $\text{H}^+$  bonded to structural  $\text{O}^{2-}$  forming  $\text{OH}^-$  groups. This H in olivine and other NAMs is generally quantified as wt. ppm  $\text{H}_2\text{O}$  and colloquially described as 'water' given that the relevant thermodynamic variable describing its incorporation is the fugacity of water ( $f_{\text{H}_2\text{O}}$ , Kohlstedt (2006)). Even at low concentrations (up to 100s wt. ppm  $\text{H}_2\text{O}$ ), water incorporated into olivine, and its magnesian end-member forsterite ( $\text{Mg}_2\text{SiO}_4$ ), can exert considerable control over the physical and chemical

properties of the crystals. Small amounts of water can lead to significant changes in strength (“hydrolytic weakening”) (Demouchy et al., 2012, Girard et al., 2013, Fei et al., 2013, Karato and Jung, 2003, Mei and Kohlstedt, 2000a, Mei and Kohlstedt, 2000b, Karato et al., 1986, Mackwell et al., 1985), texture development (Jung and Karato, 2001, Karato et al., 2008), diffusion of cations (Fei et al., 2013, Fei et al., 2018, Costa and Chakraborty, 2008, Fei and Katsura, 2016), conductivity (Fei et al., 2018, Wang et al., 2006, Sun et al., 2019), elasticity (Zhang and Xia, 2021, Jacobsen et al., 2008, Mao et al., 2010) and melting behaviour (Ueki et al., 2020).

The ability to predict and describe these changes to physical properties relies upon the ability to predict the point defect structure of hydrogen in olivine under various conditions. The mechanisms by which hydrogen can be incorporated into olivine has thus been the subject of considerable experimental study (Matveev et al., 2001, Le Losq et al., 2019, Berry et al., 2005, Tollan et al., 2018, Lemaire et al., 2004, Mosenfelder et al., 2006, Mosenfelder et al., 2011, Padron-Navarta et al., 2014, Berry et al., 2007a, Tollan et al., 2017, Blanchard et al., 2017, Jollands et al., 2021). There are also studies of the distribution of water in natural rocks (see for example Demouchy and Bolfan-Casanova (2016)) though interpretation of these is often difficult as, firstly, they typically only sample the uppermost mantle and, secondly, the rapid diffusivity of H means that rapid changes to the hydrogen concentration and its distribution could occur during magmatic ascent (Karato et al., 2008, Demouchy and Bolfan-Casanova, 2016). Despite many complexities, in general, four types of hydrated point defects have been observed. These are (using Kroger-Vink notation):  $(2H)_{Mg}^{\times}$ ,  $(4H)_{Si}^{\times}$ ,  $\{Ti_{Mg}^{\bullet\bullet}(2H)_{Si}^{\prime\prime}\}^{\times}$  and  $\{R_{Mg}^{\bullet}H_{Mg}^{\prime}\}^{\times}$  where R is a trivalent atom such as Fe(III) or Al(III) (Blanchard et al., 2017, Berry et al., 2007a). While some clear trends emerge from the literature such as  $(4H)_{Si}^{\times}$  appearing to be favoured at high pressures ( $>\sim 2$  GPa) (Smyth et al., 2006, Xue

et al., 2017, Withers and Hirschmann, 2008, Mosenfelder et al., 2006) there is no clear overall function describing how hydrogen is distributed in olivine across the upper mantle. Each experiment is performed in a limited range of conditions that generally do not cover the entire mantle range and it is hard to determine from the experimental results how different parameters such as pressure, temperature and the amount of water interact with each other to control the distribution of water within the olivine. It is also important to know not just which are the most favoured defects but the concentrations of all H-bearing defects to precise levels. This is because properties such as the diffusion of other cations (e.g.  $\text{Mg}^{2+}$  diffusion in the presence of  $(2\text{H})_{\text{Mg}}^{\times}$ ) can be affected by defects that are present even at parts-per-trillion levels due to the low concentration of intrinsic defects (Muir et al., 2020).

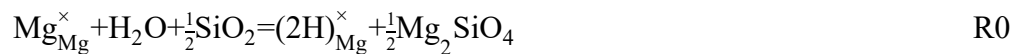
This problem can be addressed by building a thermodynamic model of hydrogen distribution in forsterite. By using *ab-initio* calculations the energy of different H-bearing and H-free defects can be determined over a wide range of conditions. Then, thermodynamic relationships can be used to determine which defects are present at what conditions. Such an approach has previously been used to consider the relationship between hydrated Si and Mg vacancies (Walker et al., 2007, Qin et al., 2018) but has not been extended to consider all likely H-bearing defects across a range of mantle conditions. In this work, we build such a thermodynamic model and probe the distribution of hydrogen in forsterite in the presence of Ti and Al. This incorporates two of the important trace elements in olivine (De Hoog et al., 2010) but excludes some potentially important elements, most notably Fe. This is because Fe introduces numerous complications to the thermodynamics and the simpler Fe-free system needs to be understood before additional complications can be considered.

## 2 Methods

### 2.1 General Method

We calculated the Gibbs free energy change associated with reactions involving a wide range of hydrous and anhydrous point defects in forsterite in order to construct a thermodynamic model of point defect distribution as a function of pressure, temperature, and chemistry. The enthalpies of isolated defects were evaluated using density functional theory (DFT) while lattice dynamics was used to determine the vibrational entropies. With the addition of analytically determined configurational entropy, these atomic scale calculations allowed us to calculate the free energy change across a series of reactions and use these to build a thermodynamic model. Minimising the Gibbs free energy at any particular set of conditions allows the equilibrium defect distribution under those conditions to be determined.

Water could incorporate into forsterite via a reaction such as:



This produces defects that bear hydrogen. We shall from now on consider water in forsterite as 'H-bearing' defects such as  $(\text{2H})_{\text{Mg}}^{\times}$  and refer to them as such. Defects lacking H are referred to as 'H-free'.

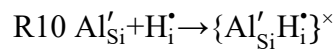
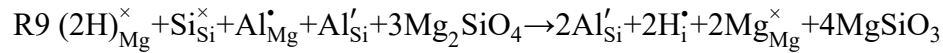
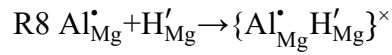
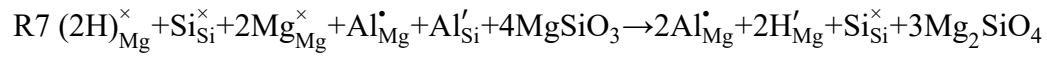
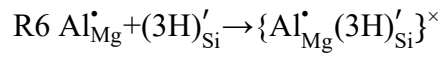
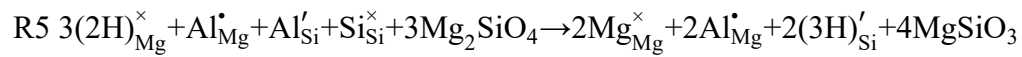
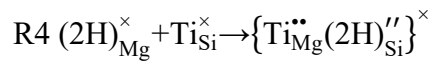
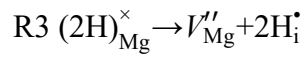
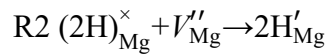
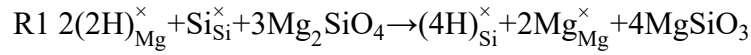
The possible H-bearing defects examined in this system are  $(\text{2H})_{\text{Mg}}^{\times}$ ,  $(\text{4H})_{\text{Si}}^{\times}$ ,

$\{\text{Ti}_{\text{Mg}}^{\bullet\bullet}(\text{2H})_{\text{Si}}^{\prime\prime}\}^{\times}$ ,  $\text{H}_{\text{Mg}}^{\prime}$  (with an  $\text{Al}_{\text{Mg}}^{\bullet}$  or free),  $\text{H}_{\text{i}}^{\bullet}$  (interstitial hydrogen bound to an O1, O2 or an O3 oxygen with a neighbouring  $\text{Al}_{\text{Si}}^{\prime}$  or free) and  $(\text{3H})_{\text{Si}}^{\prime}$  (with an  $\text{Al}_{\text{Mg}}^{\bullet}$  or free) whereas the important H-free defects are  $\text{V}_{\text{Mg}}^{\prime\prime}$ ,  $\text{Mg}_{\text{i}}^{\bullet\bullet}$  (interstitial hydrogen in I1 or I2 sites),  $\text{V}_{\text{Si}}^{\prime\prime\prime}$ ,  $\text{Al}_{\text{Mg}}^{\bullet}$ ,  $\text{Al}_{\text{Si}}^{\prime}$  and  $\text{Ti}_{\text{Si}}^{\times}$ .

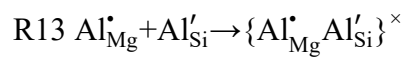
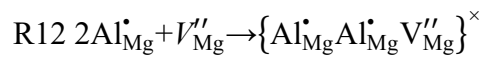
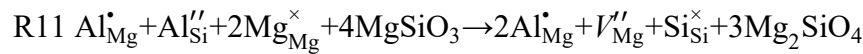
Determining the parameters of R0 is difficult due to the presence of free water.

Determining the free energy of water with sufficient accuracy at high temperature and

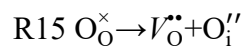
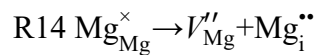
high pressure is difficult in a DFT framework due largely to its high degree of hydrogen bonding. Instead, the favoured incorporation mechanism for H in forsterite can be determined by calculating the energy differences between the different incorporation mechanisms. This was done for H-bearing defects, intrinsic defects and some selected H-free extrinsic defects. The following reactions were present in the model (all presented in Kröger-Vink notation):

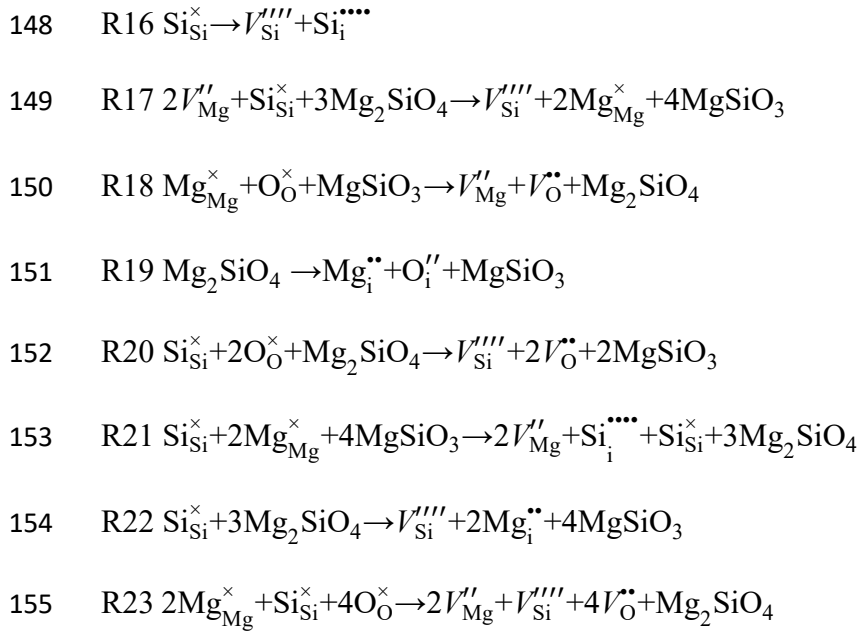


#### H-Free Extrinsic Reactions

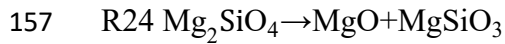


#### H-Free Intrinsic Reaction





156 Buffer Reaction



158 One important note is that we allowed the number of sites in forsterite to vary if  
 159 forsterite is created or destroyed (such as in R1 and R7) as explained in Muir et al.  
 160 (2020) but this has no noticeable effect on the results. In this formulation water starts  
 161 (arbitrarily) as  $(2\text{H})_{\text{Mg}}^{\times}$  and then reacts until it reaches its thermodynamically favoured  
 162 distribution across the various H-bearing sites. In our model the starting distribution of  
 163 hydrogen does not matter as the thermodynamic end point should always remain the  
 164 same regardless of the path it takes to reach this point as all the reactions are state  
 165 functions. In a real system the starting distribution of hydrogen and thus the source of  
 166 hydrogen does matter because of kinetic considerations but we do not consider kinetics  
 167 in our model and instead assume that the long timespans of the mantle ensure  
 168 thermodynamic equilibrium is reached. All reactions have been written as charge  
 169 balanced to ensure that the overall cell maintains electrostatic neutrality.

170 The mantle is more closely represented by an enstatite buffer and so all reactions have  
 171 been written in a system where  $\text{MgSiO}_3$  is present. These can be converted to a system

where MgO is present (or any arbitrary aSiO<sub>2</sub> value) by adding the energy of R24 in appropriate amounts.

Al was placed initially as an unbound pair of  $\text{Al}_{\text{Mg}}^{\bullet}$  and  $\text{Al}_{\text{Si}}'$ . Ti was initially placed as a 4+ cation replacing Si which is likely the major substitution mechanism of Ti in H-free forsterite (Berry et al., 2007b, Hermann et al., 2005). Defects in braces {} are defects that are locally associated with each other to form a neutral charge, this is represented in our model by placing them on adjacent sites. The concentrations of intrinsic defects are so low that the configurational entropy gain (which reduces the free energy) from randomly placing them in the crystal is much larger than the enthalpy loss (which also reduces the free energy) due to electrostatics that accompanies association of the defects (Muir et al., 2020). As an example the pairing energy of  $\{V_{\text{Mg}}''\text{Mg}_i^{\bullet\bullet}\}$ , the Mg Frenkel pair, was predicted to be 1.9 eV. In a pure system at 1500 K the enthalpy loss of binding these two defects only exceeds the entropy gain of unbinding them at pair concentrations greater than 3 ppm defects/f.u which is much larger than any Frenkel defect concentration that we predict. Thus, the intrinsic defects were always treated as isolated defects. For extrinsic defects that are produced in charge-charge pairs at much greater concentrations we allowed these to form charge-charge associated pairs if thermodynamically favourable through the reactions R6, R8, R10, R12 and R13.

## *2.2 Determining the energy of defective systems*

24 defect forming reactions are presented above. The aim was to find the concentration of defects that provides the lowest possible energy. Each reaction was assigned a reaction vector (x1...x24) between 0 and 1 which determines how far each reaction proceeds to the right between all reactants and all products. For any combination of x1-x24 we solved for the free energy (G) and the thermodynamic equilibrium was



where this free energy is minimised. Solving for the free energy consists of two parts determined as the non-configurational energy and the configurational entropy ( $S_{conf}$ ):

$$\Delta G = \sum_{i=1}^{i=24} \Delta E_i x_i - TS_{conf} \text{ Equation 1}$$

The first half of eq. 1 involves multiplying the energy (E) of each reaction at the appropriate pressure (P) and temperature (T) by its reaction vector to obtain the non-configurational energy. To determine the energy of each reaction we calculated the energy of each term in each reaction at a series of P and T points using CASTEP and the Quasi-Harmonic Approximation (QHA) with the details given in the Supplementary Methods. The second half of eq. 1 involves finding  $S_{conf}$  for any collection of defects.

$S_{conf}$  has many different components and its determination is not straightforward. We used the Gibbs entropy formula:

$$S = -k_B \sum_j p_j \ln p_j \text{ Equation 2}$$

where  $k_B$  is the Boltzmann constant,  $j$  represents a specific configuration of defects and  $p_j$  the probability that that configuration occurs. A configuration refers to a possible way in which defects are arranged across the supercell with a given concentration.

The probability of any specific configuration occurring is:

$$p_j = \frac{1}{Z} e^{(-U_j/k_B T)} \text{ Equation 3}$$

Where  $U_j$  is the internal energy of each configuration.  $Z$  in eq. 3 is the canonical partition function:

$$Z = \sum_i e^{(-U_j/k_B T)} \text{ Equation 4}$$

Strictly speaking, eq.. 3 and 4 should be calculated with  $G_j$  (the free energy of each configuration) rather than  $U_j$  (the internal energy of each configuration). This was an approximation made to allow us to calculate the energy of many different configurations quickly, as  $U$  is a lot more straightforward to calculate than  $G$ . We discuss this approximation in the supplementary information but of the defects tested

221 the largest relative difference between  $U_j$  and  $G_j$  terms was found to be in  $(4H)_{Si}^\times$  which  
 222 has geometrically very different H configurations. At 2000 K the relative difference  
 223 between  $U_j$  and  $G_j$  terms reached 0.22 eV/defect. This modification does not change  
 224 the reactions in Table 1, however, as long as the most stable defect does not change  
 225 with temperature which was found to be the case with the systems that we test. It only  
 226 changes the terms in Equations 2-4 that reflect the configurational entropy terms of  
 227 different internal geometric arrangements of each defect. These terms are proportional  
 228 to the concentration of the specific defect and thus are generally very small and thus  
 229 this approximation should not change the overall energy and distribution of hydrogen.  
 230 We also did our calculations in the dilute limit with all systems fixed to the forsterite  
 231 unit cell. This means PV terms do not vary, which reduces  $H_j$  terms to  $U_j$  ( $H=U+PV$ ).  
 232 The concentration of each defect is important because higher concentrations of each  
 233 defect lead to larger number of possible configurations ( $j$ ) (see eq. 5 below) which will  
 234 increase  $S$  in eq. 2. Therefore, we need to determine the number of configurations and  
 235 the relative enthalpy  $U_j$  of each. If we consider every possible configuration this  
 236 number quickly becomes incalculable. All configurations have a large number of other  
 237 configurations to which they are identical by the symmetry operations of the crystal  
 238 space group. By using these relationships, we defined a scheme to group configurations  
 239 into different types and thus bring the number of configurations down to a calculable  
 240 number.  
 241 We shall thus define a configuration group as a set of configurations where each of the  
 242 defects of each type is confined to a single type of site (such as all  $V_{Mg}''$  on M1 rather  
 243 than M2 sites) and we shall use these groups instead of individual configurations in eqs.  
 244 1-4. This can be conceptualised by having a single defect of each type and so the  
 245 different configuration groups simply change which site each defect occupies. With

our assumption that defects are independent, every configuration with the defects confined to a single site is identical and contained within our configuration group and configurations where defects occupy multiple sites are included by the partitioning function.  $V''_{Mg}$ ,  $H'_{Mg}$ ,  $(2H)^\times_{Mg}$  and  $Al^\bullet_{Mg}$  were confined to M1 and M2 sites,  $V''''_{Si}$ ,  $Ti^\times_{Si}$ ,  $(4H)^\times_{Si}$ ,  $(3H)'_{Si}$  and  $Al'_{Si}$  to Si sites,  $Mg^\bullet_I$  to M1 (as a split interstitial (Muir et al., 2020)) and I2 sites,  $V^\bullet_O$  and  $H^\bullet_i$  to O1, O2 and O3 sites and  $O''_I$  and  $Si^\bullet_I$  to I1, I2 and T1-T5 sites (which are defined in Muir et al. (2020)).  $\{Ti^\bullet_{Mg}(2H)''_{Si}\}^\times$ ,  $\{Al^\bullet_{Mg}Al^\bullet_{Mg}V''_{Mg}\}$ ,  $\{Al^\bullet_{Mg}(3H)'_{Si}\}^\times$ ,  $\{Al^\bullet_{Mg}H'_{Mg}\}^\times$ ,  $\{Al'_{Si}H^\bullet_i\}^\times$  and  $\{Al^\bullet_{Mg}Al'_{Si}\}^\times$  were calculated as pairs/trios with each element of the defect confined to a next or second-next neighbour site. All possible geometries of these pairs/trios were tested and considered as a separate configuration group. For defects containing hydrogen atoms each arrangement of hydrogen (hydrogen bound to a specific type of oxygen, pointing in/out of a vacancy) on each type of site was considered as a separate configuration group. The relative enthalpy of each configuration group was then calculated as a function of pressure. These enthalpies are presented in the supplement: Tables S1-S8 for H-bearing defects, Table S9-S10 for H-free defects and Table S11 for isolated defects on different crystallographic sites. For calculating the final free energy of the reactions, the most enthalpically stable configuration was chosen and its free energy calculated at high temperature. The effect of other configurations is confined to the configurational entropy term.

All possible configuration groups were then tabulated and their relative energy  $U_j$  assigned by applying energy penalties determined from the relative enthalpies in Table S1-11. The energy penalty is determined by the difference between the enthalpy of the defect in its current site with its current hydrogen arrangement compared to the enthalpy of the defect in its favored site with its favored hydrogen arrangement. This assumes

that the energy of placing and moving a defect around the crystal is independent of the other defects and that defect-defect interaction terms are minimal.

To calculate the degeneracy ( $W$ ) of each configuration group, we must first calculate the degeneracy at each site:

$$W = \ln \frac{N!}{a!b!...z!} \text{ Equation 5}$$

where  $N$  is the total number of sites, and  $a, b, c, \dots, z$  are the number of different types of atoms/defects at each site including a final  $z$  term, which is simply  $(N - a - b - \dots - y)$ . To solve this numerically, all defect concentrations were written in terms of defects per mol and then the Stirling approximation was used ( $\ln n! \cong n \ln n - n$ ), giving:

$$W = N \ln N - N - a \ln a + a - b \ln b + b \dots - z \ln z + z \text{ Equation 6}$$

Additional degeneracies from hydrogen arrangement degeneracy and the degeneracy of the bound pairs and trios were derived in a similar way and added to this term.

Knowing the degeneracy and relative energy of all configuration groups, the entropy was calculated using eqs. 2 and 3 but summed across  $i$ , where  $i$  is simply a sum across every configuration group ( $j$ ) appearing a number of times equal to its degeneracy ( $W$ ).

As the number/concentration of defects increases  $W$  increases and thus so does  $i$  and thus so does  $S$  in eq. 2.

It is important to emphasise how all the reactions R1-R24 end up coupled in determining the free energy both in this system and in defect bearing systems in general.

While the  $\sum_{i=1}^{i=24} \Delta E_i x_i$  term in eq. 1 depends upon the energetics of each reaction in isolation,  $S_{conf}$  depends upon the concentration of all defects simultaneously.  $S_{conf}$  only depends upon the concentration of the defects, the reaction by which they were produced is irrelevant. The energetics of any one reaction proceeding forwards therefore depends upon  $S_{conf}$  before and after it proceeds and thus also upon the defect concentration that is resulting from all other reactions. Thus, all reactions must be

considered simultaneously. Considering defect-producing reactions one at a time could cause incorrect defect concentrations to be obtained.

### *2.3 Thermodynamic Minimisation*

For any pressure and temperature, the energy of each defect at those conditions was determined. This was done by projecting first along pressure and then along temperature using 2<sup>nd</sup>-order polynomials and points at 5, 10 and 15 GPa (uncorrected) and 1000, 1500 and 2000 K. The energy of each defect was then placed into the reactions found in the text and the energy of each reaction ( $E_i$  in eq. 1) determined at those conditions. We then used a series of minimisations to find the distribution of defects that gave the lowest free energy by minimising  $x_1 \dots x_{24}$  in eq. 1. In all cases the water concentration, Ti concentration and Al concentration were fixed for each minimisation.

Solving this minimisation is a difficult problem as we were dealing with 24 variables that can have values that are many orders of magnitude different, multiple local minima and a configurational entropy term that has many terms and is difficult to solve analytically. Thus, we developed a bespoke solver that uses a brute force technique. This simply takes each variable ( $x_1 \dots x_{24}$ ) in their order of favourability (most favoured reactions first) and then increases or decreases that variable with a series of steps and continues to do so while  $G$  decreases. The step sizes begin at 1 and decrease to  $1 \times 10^{-20}$ . Any steps that produce negative defect concentrations were discarded. The variables were cycled through multiple times until the stopping condition, which is when a full cycle of variables ( $x_1 \dots x_{24}$ ) is changed and  $G$  fails to vary by more than a cutoff which was set to 1 peV/system. This was found to be sufficient to give consistent answers. This method relies upon the large energy differences of each of the different

reactions. R1 (the hydrated Si production reaction) is usually the most favoured reaction followed by R4 (the titanoclinohumite production reaction). The progress of other reactions have little effect on R1 and R4, while R1 and R4 have a dominant effect on the progress of other reactions. We tested this method by using a range of starting points for our minimisation (such as R1 or R4 or R7 fully to the right) and consistently arrived at the same final minimisation result. Determining concentrations of defects that are below  $1 \times 10^{-20}$  defects/f.u. proved very difficult as we encountered issues with floating point numbers and the precision of our calculations (when the other defects had much higher concentrations) and thus we used this as our baseline cutoff beyond which variables were not minimised. Our minimisation process does not present a formal solution and may miss a true energy minimum and small variations in the final concentration of the products. However, it should provide a good guide to how different conditions vary the concentration of the water products.

## *2.5 Units and visualisations*

In this work, H concentrations are always presented as wt. ppm normalised to water molecules. The overall water concentration ( $[H_2O]_{\text{bulk}}$  in wt. ppm, 1 wt. ppm =  $15.6 \text{ H/Si}$   $10^6$ ) is the sum of these concentrations for all H-bearing defects. Ti concentrations are presented as wt. ppm  $TiO_2$  and Al concentration as wt. ppm  $Al_2O_3$ . To convert to wt. ppm of Ti and Al, multiply the concentrations by 0.599 and 0.53 respectively. To account for systematic errors in DFT pressure, all pressures have been corrected with a linear method outlined in the supplementary information. Unless stated, pressures are presented as corrected.

## **3. Results**

### *3.1 Pure Forsterite*

Energies of our reactions are presented in Table 1 and Table S12. The energies of the different reactions are very different and thus the distribution of H-defects is mostly controlled by two reactions in these systems. Of the reactions involving the conversion of one H-bearing defect into a different H-bearing defect, R1 (the hydrated Si reaction which converts 2  $(2H)_{Mg}^{\times}$  into 1  $(4H)_{Si}^{\times}$ ) and R4 (the titanoclinohumite reaction which converts  $(2H)_{Mg}^{\times}$  into  $\{Ti_{Mg}^{\bullet\bullet}(2H)_{Si}^{\prime\prime}\}^{\times}$ ) are highly favoured, while the other reactions are much less favoured. Of the two most favoured reactions, the titanoclinohumite reaction R4 requires Ti and so in pure forsterite the hydrated Si reaction R1 largely controls the hydrogen distribution. The reactions which produce intrinsic defects (R14-R24) all have very high energies and thus intrinsic defects have low concentrations in these systems.

We thus predict hydrogen in pure forsterite to occupy two defects:  $(2H)_{Mg}^{\times}$  and  $(4H)_{Si}^{\times}$ .

Two other defects have been proposed in the literature (Kohlstedt, 2006) - these are

$H'_{Mg}$  and  $H_i^{\bullet}$  with the latter being an interstitial hydrogen which is bound solely to an

oxygen and not to any cationic sites. In the absence of other elements these two

defects can be produced by R2 (the Mg vacancy disproportionation reaction which

converts a  $(2H)_{Mg}^{\times}$  and a  $V''_{Mg}$  into 2  $H'_{Mg}$ ) and R3 (the free hydrogen production

reaction which converts  $(2H)_{Mg}^{\times}$  into  $H_i^{\bullet}$ ). FTIR spectra of hydrated pure forsterite

tend to show only a broad band centred at around  $3160\text{ cm}^{-1}$ , and/or a series of bands

at  $\sim 3500\text{-}3620\text{ cm}^{-1}$  (Berry et al., 2005, Grant et al., 2006) which are attributed

to  $(2H)_{Mg}^{\times}$  and  $(4H)_{Si}^{\times}$ , respectively (for example Lemaire et al. (2004)) with no

evidence for the production of  $H'_{Mg}$  and  $H_i^{\bullet}$ . Likewise, we find that  $H'_{Mg}$  and  $H_i^{\bullet}$

defects are extremely minor products. In none of our Al-free runs did the

concentration of  $H'_{Mg}$  exceed  $1 \times 10^{-20}$  defects/f.u. (the limit of detectability we set in

370 our model) and  $H_i^\bullet$  never exceeded  $1 \times 10^{-6}$  defects/f.u. in the presence of Al and  $1 \times 10^{-9}$   
 371 defects/f.u. in the absence of Al (see Figure S1 for a plot of some concentrations of  
 372  $H_i^\bullet$ ). We confirm the unfavorability of these defects by considering them as isolated  
 373 reactions in Table S13 but in summary,  $H_i^\bullet$  and  $H'_{Mg}$  are not substantially stable  
 374 products in pure H-bearing forsterite.

375 Whether  $(2H)_{Mg}^\times$  and  $(4H)_{Si}^\times$  is the dominant host of structurally bound H in forsterite  
 376 depends on pressure, temperature and water concentration. Figure 1 shows that  
 377 increasing pressure strongly encourages the formation of  $(4H)_{Si}^\times$  - almost all H is  
 378 contained in  $(4H)_{Si}^\times$  defects at pressures higher than ~3, 4 and 8 GPa at 1000, 1500 and  
 379 2000 K, respectively. This is because the hydrated Si reaction (R1) which produces  
 380  $(4H)_{Si}^\times$ , eliminates an M-site vacancy which are large and thus this reaction becomes  
 381 more favourable with increasing pressure (Table 1), e.g. at 1000 K, the reaction energies  
 382 for R1 are -1.337, -2.139 and -3.376 eV/f.u at 0, 5 and 10 GPa respectively. Previous  
 383 experimental work has shown that high pressure favours the formation of  $(4H)_{Si}^\times$   
 384 (Smyth et al., 2006, Xue et al., 2017, Withers and Hirschmann, 2008, Mosenfelder et  
 385 al., 2006). It is important to distinguish that, in Figure 1 and in our work in general, we  
 386 vary pressure independently with fixed water concentrations in the forsterite ( $[H_2O]_{bulk}$ ).  
 387 Conversely, in experimental work and in reality, increasing the pressure also increases  
 388  $fH_2O$ , and thus the water concentration in forsterite/olivine. These effects are  
 389 interlinked because, as also shown in Figure 1, increasing  $[H_2O]_{bulk}$  also stabilises  
 390  $(4H)_{Si}^\times$  over  $(2H)_{Mg}^\times$ . In general, configurational entropy terms favour  $(2H)_{Mg}^\times$  over  
 391  $(4H)_{Si}^\times$  (there are twice as many  $(2H)_{Mg}^\times$  defect sites as  $(4H)_{Si}^\times$  defect sites for the same  
 392 concentration of water) while enthalpy terms favour  $(4H)_{Si}^\times$  over  $(2H)_{Mg}^\times$  (due to R1  
 393 eliminating an unfavourable vacancy when  $(4H)_{Si}^\times$  is produced). With an increasing



394  $[\text{H}_2\text{O}]_{\text{bulk}}$  (akin to increasing  $f\text{H}_2\text{O}$  in experiments) the configurational entropy terms  
 395 become less important relative to the enthalpy terms and thus  $(4\text{H})_{\text{Si}}^{\times}$  is favoured.  
 396 Temperature favours  $(2\text{H})_{\text{Mg}}^{\times}$  over  $(4\text{H})_{\text{Si}}^{\times}$  because it multiplies the configurational  
 397 entropy term. This is shown in Figure 1 and alternatively plotted in Figure S2 where  
 398 increasing the temperature increases the proportion of  $(2\text{H})_{\text{Mg}}^{\times}$  at the same pressure and  
 399  $[\text{H}_2\text{O}]_{\text{bulk}}$ . Across a range of geophysically relevant P and T (1000-2000 K, 0-10 GPa)  
 400 P is a stronger control than T and  $(4\text{H})_{\text{Si}}^{\times}$  is the favoured H-bearing defect except at low  
 401 concentrations of water, high temperatures and low pressures. Figure S3 plots the  
 402 pressure at which  $(4\text{H})_{\text{Si}}^{\times}$  becomes favoured over  $(2\text{H})_{\text{Mg}}^{\times}$  for a variety of temperatures  
 403 – for example, at 2000 K,  $(4\text{H})_{\text{Si}}^{\times}$  becomes favoured over  $(2\text{H})_{\text{Mg}}^{\times}$  at ~8.9 GPa with a  
 404  $[\text{H}_2\text{O}]_{\text{bulk}}$  of 0.1 wt. ppm but ~4.0 GPa with a  $[\text{H}_2\text{O}]_{\text{bulk}}$  of 100 wt. ppm while at 1500 K  
 405  $(4\text{H})_{\text{Si}}^{\times}$  is the favoured water defect at all pressures when  $[\text{H}_2\text{O}]_{\text{bulk}}$  is >0.3 wt ppm.  
 406 Kudoh et al. (2006) presents a contrary case. Using electron probe microanalysis a  
 407 single crystal of hydrous forsterite with a very high amount of water (3800 wt. ppm)  
 408 that was synthesized at high pressure (13.5 GPa, 1573 K) was argued to have water  
 409 split roughly equally between Mg and Si sites. Under these conditions our model  
 410 predicts overwhelmingly water should occupy  $(4\text{H})_{\text{Si}}^{\times}$  sites. We believe that  
 411 experimental evidence of Kudoh et al. (2006) is not clear cut however. The FTIR  
 412 spectra presented in Kudoh et al. (2006) shows a strong triplet in the 3400-3600  $\text{cm}^{-1}$   
 413 region which is generally associated with  $(4\text{H})_{\text{Si}}^{\times}$  vacancies (see for example Le Losq et  
 414 al. (2019)) while the 3160-3215  $\text{cm}^{-1}$  region generally assigned to  $(2\text{H})_{\text{Mg}}^{\times}$  vacancies is  
 415 not shown but is likely flat due to its exclusion. A study by Smyth et al. (2006) in  
 416 similar conditions (12 GPa, 1273-1873 K, up to 8900 ppm wt. water) presents the FTIR  
 417 spectrum of the full 3000-3600  $\text{cm}^{-1}$  region and shows again strong absorbance in the

3400-3600  $\text{cm}^{-1}$  region and no absorbance in the 3160-3215  $\text{cm}^{-1}$  region. Thus both Smyth et al. (2006) and Kudoh et al. (2006) present FTIR spectrums in agreement with our predictions if the 3400-3600  $\text{cm}^{-1}$  region is assigned to  $(4\text{H})_{\text{Si}}^{\times}$  peaks (which it was not in either of these works) as confirmed in Xue et al. (2017) by a combination of RAMAN, NMR and theoretical calculations. The microprobe analysis of Kudoh et al. (2006) suggests the presence of hydrated water on Mg vacancies however. Assuming that the water calibration of Kudoh is correct (3800 wt. ppm) then all water cannot be on the Si vacancies as the calculated occupancy numbers (0.993 for Mg and Si respectively) fit to water distributed roughly equally between  $(4\text{H})_{\text{Si}}^{\times}$  and  $(2\text{H})_{\text{Mg}}^{\times}$  and if all water was contained in  $(4\text{H})_{\text{Si}}^{\times}$  vacancies Si occupation would be expected to be 0.986. The source of the discrepancy between our model and this experiment and between the FTIR spectrum and the microprobe results within this experiment is likely due to the extremely high water concentration. Similar to how entropically unfavoured but enthalpically favoured  $(4\text{H})_{\text{Si}}^{\times}$  is promoted by high water concentrations in our model, entropically unfavoured but (likely) enthalpically favoured grain boundary water is likely promoted by such high concentrations. The presence of grain boundary water would shift the distribution of water between Mg and Si sites in unknown directions, possibly towards Mg sites as detected by the microprobe while being absent from our model. The favourability of grain boundary water over bulk water is unknown but if we assume the enthalpy of grain boundary water is 1 eV lower than bulk water then we can estimate this favourability based on a balance of this enthalpy difference vs the configuration entropy difference (using the number of sites at the grain boundary vs in the bulk). With a circular grain with diameter of 0.05 mm we estimate that grain boundary water is  $\sim 45$  more favourable than bulk water at 1500 K. This number is very approximate but demonstrates that at such high concentrations of water grain boundary

water could be extremely important. This needs to be investigated further but in general we do not expect such high concentrations of water in the mantle and thus grain boundary water is likely unimportant and it is not present in our model.

### 3.2 The Effect of Al

There are two major H-bearing defects in the pure forsterite system,  $(4H)_{Si}^{\times}$  and  $(2H)_{Mg}^{\times}$ . The presence of Al allows the formation of a new major product  $H'_{Mg}$  which can be seen by the prominent bands at low water contents in Figure 2 and high temperatures and low pressures in Figure 3 (minor products formed in the presence of Al are shown in Figure S4 and S5). The concentration of  $H'_{Mg}$  was predicted to reach up to ~35 wt. ppm in appropriate conditions (high temperature, low pressure, low  $[H_2O]_{bulk}$ ).  $H'_{Mg}$  is produced by converting  $(2H)_{Mg}^{\times}$  to  $2H'_{Mg}$  through R7 (the Al+Mg vacancy disproportionation reaction which converts  $(2H)_{Mg}^{\times}$  and  $Al'_{Si}$  into  $H'_{Mg}$  and  $Al^{\bullet}_{Mg}$ ). R7 is more favoured than the equivalent Al-free reaction R2 (the Mg-vacancy disproportionation reaction) because it does not require a  $V''_{Mg}$  defect which are high in energy and thus difficult to produce. This reaction doubles the amount of H-bearing defects on the Mg sites (as one  $(2H)_{Mg}^{\times}$  creates two  $H'_{Mg}$  defects) but the progress of the hydrated Si reaction R1 which converts  $(2H)_{Mg}^{\times}$  to  $(4H)_{Si}^{\times}$  is unaffected by Al and so the ratio of water on Mg sites vs Si sites is unaffected by Al. This can be stated as  $2[(2H)_{Mg}^{\times}]:[(4H)_{Si}^{\times}]$  in the Al-free case is the same as  $[H'_{Mg}]:[(4H)_{Si}^{\times}]$  in the Al-bearing case. This behaviour occurs because R1 is a more favourable reaction than R7. Thus in both pure and Al-containing forsterite, the hydrated Si reaction, R1, is the controlling reaction for the distribution of water between Mg and Si sites and the presence of Al just changes the ratio  $[(2H)_{Mg}^{\times}]:[H'_{Mg}]$ . This means that the trends with pressure,

467 temperature and water concentration discussed above for pure forsterite also apply in  
 468 Al-bearing forsterite.  $H'_{Mg}$  is favoured over  $(2H)_{Mg}^{\times}$  with a low  $[H_2O]_{bulk}$  or with a high  
 469 Al concentration (Figure 2). Pressure has little effect on the  $[(2H)_{Mg}^{\times}]: [H'_{Mg}]$  ratio  
 470 while temperature favours  $(2H)_{Mg}^{\times}$  over  $H'_{Mg}$  but both of these effects are less important  
 471 than the concentration of water or Al. This can be seen in Figure 3 where we vary P  
 472 and T for a variety of water concentrations with a high Al concentration and in all cases  
 473  $H'_{Mg}$  is favoured and  $(2H)_{Mg}^{\times}$  is a very small minor product with concentrations  
 474 generally below  $1 \times 10^{-9}$  defects/f.u.. In circumstances where  $(2H)_{Mg}^{\times}$  is favoured  
 475 ( $[(2H)_{Mg}^{\times}]: [H'_{Mg}]$  is high,  $[H_2O]_{bulk}$  is high,  $[Al_2O_3]$  is low), the H distribution in Al-  
 476 bearing forsterite is near identical to Al-free forsterite.  
 477 It was stated above that Al does not affect the distribution of water in forsterite, only  
 478 converting some  $(2H)_{Mg}^{\times}$  into  $H'_{Mg}$ . This behaviour of course only applies because we  
 479 keep  $[H_2O]_{bulk}$  fixed, in real situations the addition of Al will increase the concentration  
 480 of  $[H_2O]_{bulk}$  but a fixed  $[H_2O]_{bulk}$  is important for considering how the distribution of  
 481 water is affected by the presence of Al.  
 482 In some conditions,  $H'_{Mg}$  can react further to produce  $\{Al_{Mg}^{\bullet} H'_{Mg}\}^{\times}$  through R8 (the Al  
 483 hydrated Mg vacancy coupling reaction which couples  $Al_{Mg}^{\bullet}$  and  $H'_{Mg}$ ) as shown by its  
 484 appearance as a band at high temperatures and large Al and  $[H_2O]_{bulk}$  concentrations in  
 485 Figure S4 and S5. This is always a minor product, however. With  $[H_2O]_{bulk}=100$  wt.  
 486 ppm the maximum concentration of  $\{Al_{Mg}^{\bullet} H'_{Mg}\}^{\times}$  across our PT space is  $<0.1$  wt ppm  
 487 and decreasing the water concentration will decrease this maximum. The reason this  
 488 product is always minor is because it is favoured increasingly by lower temperatures  
 489 and higher values of  $[H_2O]_{bulk}$ . This is common behaviour to all associated defect pairs  
 490 as they are favoured by enthalpy and disfavoured by  $S_{conf}$  and thus they become

491 increasingly more favoured as temperature decreases or  $[H_2O]_{\text{bulk}}$  increases. These are,  
 492 however, the same conditions that favour the formation of  $(4H)_{\text{Si}}^{\times}$ . Therefore, conditions  
 493 which favour  $\{Al_{\text{Mg}}^{\bullet} H'_{\text{Mg}}\}^{\times}$  over  $Al_{\text{Mg}}^{\bullet} + H'_{\text{Mg}}$  will also favour  $(4H)_{\text{Si}}^{\times}$  over both.  
 494  $\{Al_{\text{Mg}}^{\bullet} H'_{\text{Mg}}\}^{\times}$  is favoured over  $Al_{\text{Mg}}^{\bullet} + H'_{\text{Mg}}$  only when the concentration of both is very  
 495 small (generally less than 0.1 wt ppm) but in these cases it is possible that 100% of the  
 496  $Al_{\text{Mg}}^{\bullet} + H'_{\text{Mg}}$  pairs convert to  $\{Al_{\text{Mg}}^{\bullet} H'_{\text{Mg}}\}^{\times}$ . Across our runs we found that  $\{Al_{\text{Mg}}^{\bullet} H'_{\text{Mg}}\}^{\times}$   
 497 formed between 0-100% of the available  $H'_{\text{Mg}}$  but that generally at adiabatic mantle  
 498 temperatures  $[H'_{\text{Mg}}]$  is much larger than  $[\{Al_{\text{Mg}}^{\bullet} H'_{\text{Mg}}\}^{\times}]$ .  
 499 Berry et al. (2007a) presented the IR spectra of Al containing forsterite synthesised in  
 500 the presence of water, where a triplet of peaks in the FTIR spectra at 3344.5, 3350.5  
 501 and 3322  $\text{cm}^{-1}$  were assigned to  $\{Al_{\text{Mg}}^{\bullet} H'_{\text{Mg}}\}^{\times}$ , with the different peaks representing Al  
 502 on different sites (2 on M1, 1 on M2). Further experiments and theoretical calculations  
 503 (Blanchard et al., 2017) confirmed these assignments. In the conditions that the crystals  
 504 were annealed (1.5 GPa, 1673 K, ~100 wt. ppm  $Al_2O_3$ , saturated in water with a final  
 505 concentration of ~20 wt. ppm) we predict  $[H'_{\text{Mg}}]$  to be ~7 ppm but  $[\{Al_{\text{Mg}}^{\bullet} H'_{\text{Mg}}\}^{\times}]$  to be  
 506 <1 ppb and thus undetectable, i.e. our model is not in line with the experimental results.  
 507 The crystals were cooled, however, before spectra were recorded, and at 300 K we  
 508 predict the Al hydrated Mg vacancy coupling reaction R8 to go entirely to the right  
 509 converting all  $H'_{\text{Mg}}$  into  $\{Al_{\text{Mg}}^{\bullet} H'_{\text{Mg}}\}^{\times}$  which would create a detectable amount of  
 510  $\{Al_{\text{Mg}}^{\bullet} H'_{\text{Mg}}\}^{\times}$ . The exact amount of  $\{Al_{\text{Mg}}^{\bullet} H'_{\text{Mg}}\}^{\times}$  that is produced will be reliant on the  
 511 kinetics of the cooling process. This could be tested by recording IR spectra at high  
 512 temperature where dissociation would be expected to be observed. As can be seen from  
 513 Table S2  $\{Al_{\text{Mg}}^{\bullet} H'_{\text{Mg}}\}^{\times}$  has energetically viable arrangements where  $Al_{\text{Mg}}^{\bullet}$  can be on the

514 M1 and the M2 sites and so the assignment of the FTIR triplets in Berry et al. (2007a)  
 515 and Blanchard et al. (2017) is plausible.

516 Al can also promote minor products (pictured in Figure S4 and S5) though the  
 517 concentration of these products is always predicted to be below 1 wt. ppm. Some  $(3H)_{Si}'$   
 518 is produced through R5 (Al+Si vacancy disproportionation reaction which produces  
 519  $Al_{Mg}^{\bullet}$  and  $(3H)_{Si}'$  from  $(2H)_{Mg}^{\times}$  and  $Al_{Si}'$ ) and a small amount of  $H_i^{\bullet}$  is produced through  
 520 R9 (Al catalysed free hydrogen production which produces  $H_i^{\bullet}$  and  $Al_{Si}'$  from  $(2H)_{Mg}^{\times}$   
 521 and  $Al_{Mg}^{\bullet}$ ), though considerably more  $H_i^{\bullet}$  is produced in the presence of Al than is  
 522 produced in pure forsterite. We reiterate that  $H_{Mg}'$  is a hydrogen confined to a Mg  
 523 defect whereas  $H_{Int}^{\bullet}$  is an interstitial hydrogen that is not confined to a defect. These  
 524 two defects should have large differences in diffusional and vibrational properties and  
 525 thus have different effects on physical properties and IR spectra. These minor products  
 526  $(3H)_{Si}'$  and  $H_i^{\bullet}$  have concentrations orders of magnitude lower than the main products  
 527 of  $(2H)_{Mg}^{\times}$ ,  $H_{Mg}'$  and  $(4H)_{Si}^{\times}$  and thus will not affect the concentration of these major  
 528 products to any significant degree. The presence of these minor products will still be  
 529 important, however, for any processes that rely specifically on these defects. Both  
 530  $(3H)_{Si}'$  and  $H_{Int}^{\bullet}$  are predicted to exist as unassociated defects as  $\{Al_{Mg}^{\bullet}(3H)_{Si}'\}^{\times}$  and  
 531  $\{Al_{Si}'H_i^{\bullet}\}^{\times}$  do not form (R6 and R10 which couple the products of R5 and R9  
 532 respectively go entirely to the left) within our detectability limits ( $1 \times 10^{-20}$  defects/f.u.).  
 533 The H-free Al disproportionation reaction R11 converts  $Al_{Mg}^{\bullet} + Al_{Si}'$  into  $2 Al_{Mg}^{\bullet}$  and 1  
 534  $V_{Mg}''$ . In dry conditions this reaction can produce large amounts of  $V_{Mg}''$  leading to an  
 535 increase of the concentration of  $V_{Mg}''$  compared to pure forsterite but this reaction is  
 536 suppressed by water and is negligible beyond ~5 wt. ppm water except for very high  
 537 concentrations of Al. This can be seen in Figure 4 where the steep decline in  $[V_{Mg}'']$

with increasing  $[H_2O]_{\text{bulk}}$  signifies the suppression of this reaction. Discussion of the  $\{Al_{Mg}^{\bullet}Al_{Mg}^{\bullet}V_{Mg}''\}$  cluster is given in the supplementary information but generally it is an extremely minor product (concentrations are always below  $2 \times 10^{-15}$  defects/f.u.) which is not expected to be important.

Defects interacting with Al can change the ratio of  $Al_{Mg}^{\bullet}/Al_{Si}'$  from its initial value of 1 in multiple possible reactions (R5, R7, R9, R11). We find that this effect is mostly controlled by the Al+Mg vacancy disproportionation reaction R7 ( $(2H)_{Mg}^{\times}$  and  $Al_{Si}'$  into  $H_{Mg}'$  and  $Al_{Mg}^{\bullet}$ ). This ratio is listed as a function of water concentration in Table S14. We find that H-induced changes to this ratio are generally small with  $[Al_{Mg}^{\bullet}]$  usually being  $<0.1\%$  larger than  $[Al_{Si}'']$  but at high temperatures, low pressures, low Al contents and high water contents the  $Al_{Mg}^{\bullet}/Al_{Si}'$  ratio can become significant. In such conditions, measuring two of the water content, the Al content and the  $Al_{Mg}^{\bullet}/Al_{Si}'$  value would allow you to know the other value.

In the absence of any other reactions Al exists as  $Al_{Mg}^{\bullet} + Al_{Si}'$  pairs which could associate into  $\{Al_{Mg}^{\bullet}Al_{Si}'\}^{\times}$  through R13 (Al pair coupling reaction). We predict that the favourability of this reaction is highly dependent upon pressure, temperature and Al concentration and that  $\{Al_{Mg}^{\bullet}Al_{Si}'\}^{\times}$  associated pairs make up anywhere between 1.01 to 99.81% of the total  $Al_{Mg}^{\bullet} + Al_{Si}'$  pairs with the remaining percentage being unbound. Lower temperatures, higher Al concentrations and higher pressures lead to a greater percentage of  $\{Al_{Mg}^{\bullet}Al_{Si}'\}^{\times}$  pairs being bound, with water concentration having little effect.

### 3.3 The Effect of Ti

As shown in Figure 2, Ti has a large effect on the distribution of H through the formation of  $\{Ti_{Mg}^{\bullet}(2H)_{Si}''\}^{\times}$  via the titanoclinohumite reaction R4 which is very

562 favourable (Table 1).  $\{\text{Ti}_{\text{Mg}}^{\bullet\bullet}(\text{2H})_{\text{Si}}''\}^{\times}$  is favoured versus  $(\text{4H})_{\text{Si}}^{\times}$  at low pressures and  
 563 versus  $(\text{2H})_{\text{Mg}}^{\times}$  at low temperatures and thus can be the major product at low pressures  
 564 and temperatures as seen by the large band at low pressures in Figure 3. With increasing  
 565 pressure  $(\text{4H})_{\text{Si}}^{\times}$  becomes more stable than  $\{\text{Ti}_{\text{Mg}}^{\bullet\bullet}(\text{2H})_{\text{Si}}''\}^{\times}$  as was also the case with  
 566  $(\text{2H})_{\text{Mg}}^{\times}$ , but  $\{\text{Ti}_{\text{Mg}}^{\bullet\bullet}(\text{2H})_{\text{Si}}''\}^{\times}$  is generally stable to a higher pressure against  $(\text{4H})_{\text{Si}}^{\times}$  than  
 567  $(\text{2H})_{\text{Mg}}^{\times}$ . This is shown in Figure S3 where the presence of Ti increases the pressure at  
 568 which  $(\text{4H})_{\text{Si}}^{\times}$  becomes the dominant water carrier by up to 2 GPa at 2000 K and by up  
 569 to 7 GPa at 1500 K. A conversion of  $\{\text{Ti}_{\text{Mg}}^{\bullet\bullet}(\text{2H})_{\text{Si}}''\}^{\times}$  to  $(\text{4H})_{\text{Si}}^{\times}$  with pressure has been  
 570 observed previously as Kohlstedt et al. (1996) showed FTIR peaks associated to  
 571  $\{\text{Ti}_{\text{Mg}}^{\bullet\bullet}(\text{2H})_{\text{Si}}''\}^{\times}$  in crystals annealed at 0.3 GPa but only those associated with  $(\text{4H})_{\text{Si}}^{\times}$  in  
 572 crystals annealed at 5 GPa though these peaks were not interpreted as such within this  
 573 paper.

574 The binding energy (energy of associated defect minus the energy of isolated defects)  
 575 of  $\{\text{Ti}_{\text{Mg}}^{\bullet\bullet}(\text{2H})_{\text{Si}}''\}^{\times}$  was calculated to be extremely large (between 5-6 eV between 0-15  
 576 GPa and 0-2000 K) and thus  $\{\text{Ti}_{\text{Mg}}^{\bullet\bullet}(\text{2H})_{\text{Si}}''\}^{\times}$  is almost always an associated pair. Only  
 577 at an extremely low concentrations (<1 ppt wt.) would disassociating this pair be  
 578 favourable. In our model we always treated this as an associated pair.

579 As with Al, the site location of Ti is related to the water content. As shown in Table  
 580 S15 the  $\text{Ti}_{\text{Si}}^{\times}/\text{Ti}_{\text{Mg}}^{\bullet\bullet}$  ratio decreases roughly linearly with water content for a given P and  
 581 T. The ratio varies strongly and nonlinearly with P and T, however, so fitting a universal  
 582 law is complex and will have overlapping points but with a known P and T the water  
 583 content can be solved from the  $\text{Ti}_{\text{Si}}^{\times}/\text{Ti}_{\text{Mg}}^{\bullet\bullet}$  ratio. This provides both a test of unknown



water content if this ratio can be measured and a test of our model if the water content is known.

In Table S16 we compare our model data with a model produced from experimental data (Padron-Navarta and Hermann, 2017). We find a good match between their model and our prediction within the experimental region but an increasingly large mismatch outside of this region due to the absence of  $(2\text{H})_{\text{Mg}}^{\times}$  in the experimental measurements. This absence is because the experimental measurements were done at low temperatures (1023-1323 K) where we predict that  $(2\text{H})_{\text{Mg}}^{\times}$  does not form and thus would not be seen in the experiment. This is evidence that extrapolating outside measured T and P regions (and  $[\text{H}_2\text{O}]_{\text{bulk}}$  and trace element concentration ranges) is very difficult as different H-bearing defects can form when you change these variables. The predicted concentration of  $\{\text{Ti}_{\text{Mg}}^{\bullet\bullet}(\text{H})_{\text{Si}}^{\prime}\}^{\times}$ , however, always remains within 10 ppm between our model and their model.

## 4. Discussion

### 4.1 Water exponents of intrinsic defects

Many experimental studies have related the incorporation of  $\text{H}_2\text{O}$  into point defects in olivine and other NAMs using the water fugacity ( $f\text{H}_2\text{O}$ ) of the system and an exponent ( $rf$ ), i.e.:

$$[\text{Defect}] \propto f_{\text{H}_2\text{O}}^{rf} \quad \text{Equation 8}$$

(Kohlstedt et al., 1996, Withers et al., 2011, Tollan et al., 2017, Withers and Hirschmann, 2007, Rauch and Keppler, 2002, Mierdel and Keppler, 2004, Lu and Keppler, 1997, Bromiley and Keppler, 2004). The experimental method generally involves either varying P at constant T and water activity ( $a\text{H}_2\text{O}$ ), thus varying  $f\text{H}_2\text{O}$ , or varying  $a\text{H}_2\text{O}$  (and thus  $f\text{H}_2\text{O}$ ) at constant P and T, with both methods allowing the

relationship between defect concentrations and  $f_{\text{H}_2\text{O}}$  to be determined. In simple systems where each product can be described by a single equation (such as  $(4\text{H})_{\text{Si}}^{\times}$  being solely produced by the hydrated Si production reaction R1) and where configurational entropy is unimportant, each product can indeed be described by a single number ( $rf$ ) which should be relatively insensitive to pressure, temperature and water concentration.

In complex systems  $rf$  will often vary significantly with conditions such as P and T.

In our calculations we do not have  $f_{\text{H}_2\text{O}}$  but can instead determine

$$[\text{Defect}] \propto [\text{H}_2\text{O}]_{\text{bulk}}^{rc} \quad \text{Equation 9}$$

Herein, all calculated exponents are  $rc$ , as in eq. 9 rather than  $rf$  as in eq. 8. While eqs. 9 and 8 have occasionally been treated as the same in previous literature (such as in Fei and Katsura (2016)) they are not, as eq. 9 has additional implicit configurational entropy mixing terms that are not present in eq. 8. These terms vary based on the form water takes when adsorbed in the system but stem from the fact that  $[\text{H}_2\text{O}]_{\text{bulk}}$  is not a real product and these are the terms that mix  $\text{H}_2\text{O}$  to whatever configuration it takes in forsterite. The effect of this is varied and  $rc$  can be equal to, greater than or less than  $rf$ . For eq. 9 the dominant water defect (the species that contains most of the water and controls the charge balance regime) in forsterite should have an  $rc$  that trends towards 1 while the exponents of the other water species are (in a simple system) dependent on how the minor water species relate to the major species. An example demonstrating how to calculate the “ideal” value of  $rc$  and the relationship between  $rf$  and  $rc$  is given in the supplementary information for reaction R1.

Our predicted  $rc$  values are given in Table 2. The values of  $rc$  are quite variable and often do not have their ideal value. As an example in the case of pure forsterite with no trace elements except H the  $rc$  value for  $(2\text{H})_{\text{Mg}}^{\times}$  at 0 GPa varies between 0.5 to 0.82 with temperature. The “ideal” value is 0.5 in a  $(4\text{H})_{\text{Si}}^{\times}$  dominated system and 1 in a

(2H)<sub>Mg</sub><sup>x</sup> dominated system and it varies between these. Thus we predict that water exponents in “real” systems should be heavily dependent upon pressure, temperature and chemical environment, and that they can also vary across common ranges in H<sub>2</sub>O concentration. Particularly large variations in  $rc$  are seen when the major H-bearing defect changes from (2H)<sub>Mg</sub><sup>x</sup> to (4H)<sub>Si</sub><sup>x</sup>. This can be seen in Table 2 where at high temperature and low pressures (which favours (2H)<sub>Mg</sub><sup>x</sup>)  $rc$  for (2H)<sub>Mg</sub><sup>x</sup> is 0.82 and  $rc$  for (4H)<sub>Si</sub><sup>x</sup> is 1.63 (at 2000 K and 0 GPa respectively) but as temperature decreases and pressure increases (which favours (4H)<sub>Si</sub><sup>x</sup>) these values instead trend towards and become (at 10 GPa and 1000 K) 0.50 and 1.00 respectively. The exponents for (2H)<sub>Mg</sub><sup>x</sup> and (4H)<sub>Si</sub><sup>x</sup> always have a roughly 1:2 ratio because [(4H)<sub>Si</sub><sup>x</sup>] is controlled by the hydrated Si production reaction R1.

#### 4.2 Exponents of intrinsic defects

The presence of water will also have a large effect on the concentration of intrinsic defects in forsterite. In general, the presence of water is seen to suppress the formation of intrinsic defects. As shown in Figure 4 increasing [H<sub>2</sub>O]<sub>bulk</sub> generally decreases the concentration of defects produced intrinsically. This is because intrinsic defects in forsterite (and generally in minerals) form due to configurational entropy gains upon formation, and these gains become relatively lowered in the presence of H-bearing defects (or other extrinsic defects).

Each atom in Mg<sub>2</sub>SiO<sub>4</sub> has an equivalent vacancy and interstitial defect. Mg vacancies ( $V''_{Mg}$ ) and Mg interstitials ( $Mg_i^{''}$ ) are the most prominent intrinsic defects due to the favourability of the Mg Frenkel reaction (R14) over other intrinsic reactions (Table S12).  $V_O^{''}$  is the next most prominent intrinsic vacancy (formed in conjunction with  $V''_{Mg}$

658 in R18) and then  $V_{\text{Si}}''''$  (formed by converting  $2V_{\text{Mg}}''$  into  $V_{\text{Si}}''''$  in the vacancy Si  
 659 production reaction R17, a H-free analogy to the hydrated Si production reaction R1).  
 660 We predict that  $V_{\text{Si}}''''$  is produced entirely by R17 and not by any of the other possible  
 661  $V_{\text{Si}}''''$ -forming reactions, which have much higher energies (Table S12). Therefore, the  
 662 concentration of  $V_{\text{Si}}''''$  is proportional to the concentration of  $V_{\text{Mg}}''$ , which is a reactant in  
 663 the vacancy Si production reaction R17. Previous thermodynamic models have used  
 664 the Si Frenkel reaction (R16) as a basis for forming  $V_{\text{Si}}''''$  (Stocker and Smyth, 1978)  
 665 and therefore came to different conclusions about the effect of various conditions on  
 666  $V_{\text{Si}}''''$ . However, we find the formation of  $V_{\text{Si}}''''$  via R16 to be extremely unfavourable.  
 667 No mechanism that we tested which produces  $O_i''$  or  $\text{Si}_i''''$  was favourable - the  
 668 concentration of these defects was always below the detection limit ( $1 \times 10^{-20}$   
 669 defects/f.u.) and likely far below this limit based on the extremely high energies of all  
 670 reactions that produce these interstitials. We therefore conclude that Si and O  
 671 interstitials are not present in forsterite to any significant degree. In Costa and  
 672 Chakraborty (2008) it was predicted that in olivine Si diffuses via a vacancy mechanism,  
 673 which agrees with our results, but that O diffuses via an interstitial method which does  
 674 not. We predict that R18 which produces  $V_{\text{O}}''$  (alongside  $V_{\text{Mg}}''$ ) is always more favoured  
 675 than the reactions which produce  $O_i''$  (R15 and R22). Thus we predict that it is difficult  
 676 to produce  $O_i''$  in forsterite and that a  $V_{\text{O}}''$  mechanism is more likely for O diffusion  
 677 unless an external source of  $O_i''$  is present.  
 678 The effect of water on exponents associated with intrinsic defects has been previously  
 679 speculated in Kohlstedt (2006). Using similar mass action equations to R0, R1 and R17  
 680 (as well as variations on these to consider alternative Mg water sites and Si hydrogen  
 681 concentrations) and the effect of water on the equilibrium constants of these reactions  
 682 (as demonstrated in the supplementary information) they postulated that water has no

683 effect on  $V''_{\text{Mg}}$  and  $V'''_{\text{Si}}$  (i.e.  $rc=rf=0$ ) in the charge balance regime  $[H^*]=[H'_{\text{Me}}]$ , where  
 684 their  $H'_{\text{Me}}$  is effectively equivalent to our  $H'_{\text{Mg}}$ . This line of reasoning was extended to  
 685 O vacancies  $V^{\bullet\bullet}_{\text{O}}$  by Fei and Katsura (2016) who used similar arguments to postulate  
 686 that  $rc=rf=0$  ie  $[V^{\bullet\bullet}_{\text{O}}] \propto [H_2O]_{\text{bulk}}^0 \propto fH_2O^0$ . We find, however, that generally these  
 687 products can have negative  $rc$  (Table 2) due to the suppressive effect of water on their  
 688 configurational entropy of formation. The exponent of  $V''_{\text{Mg}}$  is sometimes positive due  
 689 to the effects of the free hydrogen production reaction R3 which creates  $V''_{\text{Mg}}$  and  $H^{\bullet}_i$ .  
 690 While R3 only proceeds forwards by a small amount and produces low  $[V''_{\text{Mg}}]$   
 691 compared to the concentration of other extrinsically produced defects,  $[V''_{\text{Mg}}]$  produced  
 692 by R3 can be much higher than  $[V''_{\text{Mg}}]$  produced intrinsically through the Mg Frenkel  
 693 reaction R14. We cannot determine  $rc$  for  $V'''_{\text{Si}}$  directly because the concentration of  
 694  $V'''_{\text{Si}}$  is extremely low and often below our detection limit. However, as the  
 695 concentration of  $V'''_{\text{Si}}$  is controlled entirely by the Si vacancy production reaction R14  
 696  $rc$  for  $V'''_{\text{Si}}$  should be close to twice the  $rc$  of  $V''_{\text{Mg}}$ .  
 697 We find that water can have significant effects on the concentrations of  $V''_{\text{Mg}}$ ,  $V'''_{\text{Si}}$   
 698 and  $V^{\bullet\bullet}_{\text{O}}$ , particularly in the presence of Al and Ti, which is contrary to their predicted  
 699 ideal behaviour where the concentration of water should have no effect. This is  
 700 unsurprising as configurational entropy (which causes deviations from these ideal  
 701 values) will always be important for intrinsic defects, as it is fundamental to their  
 702 creation. All of the intrinsic defect-forming reactions have high positive enthalpies  
 703 meaning that they only proceed forwards due to the configurational entropy gain of  
 704 producing defects. Therefore, in most scenarios, the exponents for intrinsic defects will  
 705 be heavily sensitive to configurational entropy and will deviate from their ideal values.  
 706 Effectively, this means that when dealing with intrinsic defects their exponents ( $rc$  and

rf) are particularly hard to extrapolate across temperature and pressure space and must be measured at the desired conditions.

### 4.3 The distribution of water in upper mantle conditions

As discussed above, the distribution of hydrogen in forsterite is highly complex with multiple interacting variables that defy simple parameterisation and that each set of pressure and temperature conditions could behave differently. In this section, we want to show how the H-bearing defects behave in a set of geophysically relevant pressure and temperature conditions, i.e. those of the upper mantle. Figure 5 and 6 (with alternative renderings in Figure 7 and S6-S9) show the distribution of H-bearing defects along two likely mantle geotherms (taken from Green and Ringwood (1970)) with varying Ti and Al concentrations. In Figure 7 and S6-S9 the concentrations of Ti and Al are both correlated with depth based on De Hoog et al. (2010) but there is simply an example and in reality there is likely considerable variation in the concentration of both of these products. In Figure 5 we show the variation of these two concentrations separately. Figure 5, 6 and 7 either have a varying water concentration with depth (Figure 5 and 7) using a fit to natural samples from Demouchy and Bolfan-Casanova (2016) (Table S16) or a fixed water concentration with depth (Figure 6). While water, Ti and Al concentrations are likely strongly correlated with depth they are also possibly laterally heterogeneous and in this way we can demonstrate how varying the concentration of these products varies the distribution of H regardless of depth.  $H'_{Mg}$  likely has similar diffusional and other properties to  $(2H)_{Mg}^{\times}$  and thus we shall consider them together with a combined concentration  $[H+V_{Mg}]$ .

Overall, we conclude that depth (and thus pressure) is the most important variable in distributing H in the mantle. In Figure 5, 6 and 7 an overall trend with depth can be seen regardless of other conditions. Considering first  $[H+V_{Mg}]$ , this has a near-0 value

732 at the surface which rises rapidly with depth, peaks in the mid upper mantle (seen by  
 733 the middling yellow band in Figure 5 and 6) and then decreases rapidly. This peak is  
 734 tabulated in Table S18 but is at 100-210 km with shallower values favoured by higher  
 735 temperatures. Even at this peak concentration, hydrated Mg vacancies  $((2H)_{Mg}^{\times}$  and  
 736  $H'_{Mg}$ ) never become the dominant H-bearing defect. This behaviour is effectively  
 737 insensitive to Ti concentration with the main effect of Ti being to reduce the maximum  
 738 value of  $[H+V_{Mg}]$  at its peak (Figure 7 and Table S18). Ti has a strong effect on  $[(4H)_{Si}^{\times}]$   
 739 however and so we shall consider a Ti-poor and a Ti-rich regime. An important value  
 740 is the saturation concentration which is  $[TiO_2] \sim 4.42 \times [H_2O]_{bulk}$ . This is the  
 741 concentration at which there is enough Ti for all water molecules to form  $\{Ti_{Mg}^{\bullet\bullet}(2H)_{Si}^{\prime\prime}\}^{\times}$ .  
 742 With low Ti concentrations ( $[TiO_2] < \text{saturation}$ )  $[(4H)_{Si}^{\times}]$  is predicted to be the  
 743 dominant H-bearing phase throughout the lower mantle and its concentration is nearly  
 744 equal to  $[H_2O]_{bulk}$  regardless of depth. Thus if  $[H_2O]_{bulk}$  increases with depth (Figure 5)  
 745 so does  $[(4H)_{Si}^{\times}]$  and if  $[H_2O]_{bulk}$  is fixed with depth (Figure 6)  $[(4H)_{Si}^{\times}]$  is also fixed  
 746 with depth. This can be seen most clearly in the  $[TiO_2]=0$  regions of Figure 6 where  
 747  $[(4H)_{Si}^{\times}]$  does not change with depth. In these Ti-poor cases the minimum concentration  
 748 of  $(4H)_{Si}^{\times}$  is when  $[H+V_{Mg}]$  is at its maximum in the mid mantle. With a  $[H_2O]_{bulk}$  of  
 749 1/10/100/1000 wt. ppm the minimum  $[(4H)_{Si}^{\times}]$  is 0.2/6.3/85.4/966 wt. ppm while the  
 750 maximum  $[(4H)_{Si}^{\times}]$  is 1/10/100/1000 wt. ppm. Thus, in a hypothetical (likely  
 751 unrealistic) Ti-poor system, variations in  $[(4H)_{Si}^{\times}]$  throughout the conditions of the  
 752 upper mantle are small and decrease with  $[H_2O]_{bulk}$ . With high Ti concentrations  
 753 ( $[TiO_2] > \text{saturation}$ ) very different behaviour is seen. In these regions a large band  
 754 exists at the top of the upper mantle where  $\{Ti_{Mg}^{\bullet\bullet}(2H)_{Si}^{\prime\prime}\}^{\times}$  is the dominant H-defect  
 755 and  $[(4H)_{Si}^{\times}]=0$  (the blue band in the Ti-regions of the  $(4H)_{Si}^{\times}$  diagram of Figure 5 and

756 6).  $[(4H)_{Si}^{\times}]$  remains effectively at 0 until ~40 km in oceanic mantle and ~80 km in  
 757 continental mantle and then steadily increases with depth, overtakes Ti to be the  
 758 dominant H-defect at around ~100-250 km and reaches its Ti-free value at around 250-  
 759 300 km along both oceanic and continental geotherms.  $[\{Ti_{Mg}^{\bullet\bullet}(2H)_{Si}^{\prime\prime}\}^{\times}]$  generally  
 760 decreases slightly (fixed  $[H_2O]_{bulk}$ ) or increases slightly (variable  $[H_2O]_{bulk}$ ) with depth  
 761 until ~200 km when its concentration drops rapidly with depth in favour of  $[(4H)_{Si}^{\times}]$ .  
 762 This overall trend with depth is quite robust in the face of all other variables.  
 763  $[Al_2O_3]$  has no large effect on the distribution of the major products as discussed above  
 764 and which can be seen in the Ti=0 sections of Figure 5 which are largely homogenous  
 765 with varying Al content.  $[TiO_2]$  has a big effect on H distribution as explained above  
 766 but this effect quickly saturates. When  $[TiO_2] < \text{saturation}$  the effect of  $[TiO_2]$  is largely  
 767 linear as  $\{Ti_{Mg}^{\bullet\bullet}(2H)_{Si}^{\prime\prime}\}^{\times}$  is strongly favoured and thus forms linearly with increasing  
 768  $[TiO_2]$ . This can be seen in Figure 5 and 6 by a smooth colour change along the  $[TiO_2]$   
 769 concentration gradients before the saturation point is reached and the colour no longer  
 770 changes. When  $[TiO_2] > \text{saturation}$ , varying the Ti concentration has no effect as seen  
 771 by the regions in Figure 5 and 6 where  $[TiO_2]$  varies. At deep depths  $(4H)_{Si}^{\times}$  is favoured  
 772 and the value of  $[TiO_2]$  is largely irrelevant. Increasing  $[H_2O]_{bulk}$  favours  $[(4H)_{Si}^{\times}]$  and  
 773 suppresses  $[\{Ti_{Mg}^{\bullet\bullet}(2H)_{Si}^{\prime\prime}\}^{\times}]$  in the upper mantle but very high concentrations of water  
 774 are needed before  $[\{Ti_{Mg}^{\bullet\bullet}(2H)_{Si}^{\prime\prime}\}^{\times}]$  is suppressed significantly. This can be seen in  
 775 Figure 6 where at 10 wt. ppm water the value of  $[(4H)_{Si}^{\times}]$  at shallow depths is very  
 776 dependent on  $[TiO_2]$  (the blue band) but at 100 wt. ppm water only very high values  
 777 of  $[TiO_2]$  affect  $[(4H)_{Si}^{\times}]$  (the blue band forms at much higher concentrations of  $[TiO_2]$ ).  
 778 At 1000 wt. ppm  $\{Ti_{Mg}^{\bullet\bullet}(2H)_{Si}^{\prime\prime}\}^{\times}$  is effectively suppressed and  $[(4H)_{Si}^{\times}]$  is effectively  
 779 insensitive to  $[TiO_2]$ . As seen by the difference between H-distributions along oceanic



and continental geotherms in Figure 5 different temperatures have a small effect on H distribution. This mostly affects  $[H+V_{Mg}]$  which should be much larger in hotter mantle (Table S18). This shows however that temperature fluctuations in the mantle can be important. All of these effects are small compared to the effect of depth, however, and mostly shift the changes seen with depth rather than suppress them.

Overall we find that across mantle pressures and temperatures that there are multiple different H-bearing defect regimes and that there is no one uniform H distribution that can be applied across the upper mantle. Aside from depth, lateral variations in temperature or the concentrations of Ti or water could cause large changes in H distribution. This means that when modelling the effect of water on upper mantle forsterite properties, multiple equations are likely required to represent mantle heterogeneity and depth. The large variation in the distribution of H with depth would be difficult to predict from measurements which only modify a single variable or which sample only small regions of P and T space and which only measure most prominent H-defects. The coupling of T and P is particularly important in controlling the  $[H+V_{Mg}]$ :  $[(4H)_{Si}^{\times}]$  ratio as this ratio is increased by the former and decreased by the latter and thus the shape of the geotherm will control the shape and depth of the  $[H+V_{Mg}]$  spike. In upper mantle conditions, however, we find P to be overwhelmingly the most important variable and thus when considering the H distribution in forsterite a range of pressures must be examined.  $[H_2O]_{bulk}$  is an important secondary variable (for relative concentrations, for absolute concentrations it is of critical importance) and experimental studies on saturated forsterite may over-represent  $[(4H)_{Si}^{\times}]$  (which is favoured by high  $[H_2O]_{bulk}$ ) when compared to mantle forsterite which will likely be undersaturated. Properties such as forsterite conductivity (Sun et al., 2019, Fei et al.,

2018) and strength (Demouchy and Bolfan-Casanova, 2016) are partially functions of  $[H+V_{Mg}]$  and  $[(4H)_{Si}^{\times}]$  respectively and have different relations with  $[H_2O]_{bulk}$  and  $fH_2O$  in different conditions that could be encountered in the upper mantle and thus the effect of water on these properties cannot be modelled with a single exponent as has been previously attempted.

We have not considered the effect of Fe in these systems but the complex relationship between the defects likely holds in the presence of Fe. The main effect of iron is likely that it introduces a competing reaction which forms  $\{Fe_{Mg}^{\bullet}H'_{Mg}\}^{\times}$ . This could be the main H-bearing defect under various conditions (Berry et al., 2007a) but is unlikely to affect the fundamental relationships between  $[H+V_{Mg}]$ ,  $[(4H)_{Si}^{\times}]$  and  $[Ti_{Mg}(2H)_{Si}^{\prime\prime}]^{\times}$  described here and will likely simply scale the values of these concentrations down while they maintain their internal depth dependence. Iron will also make the system more sensitive to  $fO_2$  fluctuations which have been ignored in this work due to them not having an obvious effect on forsterite chemistry. The presence of Fe will make this system more complex and thus will further the overall conclusion that the distribution of H in forsterite/olivine is very complex and very sensitive to conditions. Other elements that could be present in the mantle and that interact strongly with hydrogen such as fluorine (Crepisson et al., 2014) and boron (Kent and Rossman, 2002) will further increase complexity and need to be considered further.

## 5. Conclusions

In conclusion we built a thermodynamic model of hydrogen distribution in forsterite from first principles. We find that even for a very simple system (pure forsterite plus three trace elements) a very complex model is required to correctly predict hydrogen distribution. In different pressure, temperature, water fugacity and trace element

regimes different H-bearing defects can be favoured and the effect of water fugacity will be different as seen through differing  $rc$  and  $rf$  values in different pressure and temperature regimes. Extrapolating properties such as the concentration of H-bearing defects and the water exponents ( $rc$  and  $rf$ ) between these regimes is extremely difficult and thus only results in the desired regime should be used when considering H distribution in forsterite. This has effects both on building models for the upper mantle where multiple constraints are required on the effect of water and on experiments where high water fugacities may overstate the effect of  $(4H)_{Si}^{\times}$  and where derived H-defect concentrations and water exponents may be reflective of only very narrow ranges of pressure and temperature space.

To move towards a full understanding of the effect of water in olivine in the upper mantle more elements need to be considered. Iron is an obvious choice for consideration but it is important to establish which elements can form H-bearing defects that can be examined. Elements like Ni are reasonably abundant in olivine but lack obvious associated H-bearing defects whereas elements like Cr are less abundant but could form H-bearing defects such as via the 3+ oxidation state of Cr. Each additional element will increase the complexity of the models here and thus the effect of hydrogen in real olivine in the lower mantle is likely to be very complex and water likely has different effects on the properties of olivine in different parts of the upper mantle.

Acknowledgments:

Funding was provided by National Natural Science Foundation of China (41773057, 42050410319), and by the National Environment Research Council as part of the Volatiles, Geodynamics and Solid Earth Controls on the Habitable Planet research programme

(NE/M000044/1). JM is highly thankful to Chinese Academy of Sciences (CAS) for PIFI. We would like to thank two anonymous reviewers for very helpful reviews.

#### Statements and Declarations:

The authors declare no competing interests

#### Bibliography

- BERRY, A. J., HERMANN, J., O'NEILL, H. S. C. & FORAN, G. J. 2005. Fingerprinting the water site in mantle olivine. *Geology*, 33, 869-872.
- BERRY, A. J., O'NEILL, H. S. C., HERMANN, J. & SCOTT, D. R. 2007a. The infrared signature of water associated with trivalent cations in olivine. *Earth and Planetary Science Letters*, 261, 134-142.
- BERRY, A. J., WALKER, A. M., HERMANN, J., O'NEILL, H. S., FORAN, G. J. & GALE, J. D. 2007b. Titanium substitution mechanisms in forsterite. *Chemical Geology*, 242, 176-186.
- BLANCHARD, M., INGRIN, J., BALAN, E., KOVACS, I. & WITHERS, A. C. 2017. Effect of iron and trivalent cations on OH defects in olivine. *American Mineralogist*, 102, 302-311.
- BROMILEY, G. D. & KEPPLER, H. 2004. An experimental investigation of hydroxyl solubility in jadeite and Na-rich clinopyroxenes. *Contributions to Mineralogy and Petrology*, 147, 189-200.
- COSTA, F. & CHAKRABORTY, S. 2008. The effect of water on Si and O diffusion rates in olivine and implications for transport properties and processes in the upper mantle. *Physics of the Earth and Planetary Interiors*, 166, 11-29.
- CREPISSE, C., BLANCHARD, M., BUREAU, H., SANLOUP, C., WITHERS, A. C., KHODJA, H., SURBLE, S., RAEPSAET, C., BENEUT, K., LEROY, C., GIURA, P. & BALAN, E. 2014. Clumped fluoride-hydroxyl defects in forsterite: Implications for the upper-mantle. *Earth and Planetary Science Letters*, 390, 287-295.
- DE HOOG, J. C. M., GALL, L. & CORNELL, D. H. 2010. Trace-element geochemistry of mantle olivine and application to mantle petrogenesis and geothermobarometry. *Chemical Geology*, 270, 196-215.
- DEMOUCHY, S. & BOLFAN-CASANOVA, N. 2016. Distribution and transport of hydrogen in the lithospheric mantle: A review. *Lithos*, 240, 402-425.
- DEMOUCHY, S., TOMMASI, A., BAROU, F., MAINPRICE, D. & CORDIER, P. 2012. Deformation of olivine in torsion under hydrous conditions. *Physics of the Earth and Planetary Interiors*, 202, 56-70.
- FEI, H., WIEDENBECK, M., YAMAZAKI, D. & KATSURA, T. 2013. Small effect of water on upper-mantle rheology based on silicon self-diffusion coefficients. *Nature*, 498, 213-+.
- FEI, H. Z. & KATSURA, T. 2016. Si and O self-diffusion in hydrous forsterite and iron-bearing olivine from the perspective of defect chemistry. *Physics and Chemistry of Minerals*, 43, 119-126.
- FEI, H. Z., KOIZUMI, S., SAKAMOTO, N., HASHIGUCHI, M., YURIMOTO, H., MARQUARDT, K., MIYAJIMA, N. & KATSURA, T. 2018. Mg lattice diffusion in iron-free olivine and implications to conductivity anomaly in the oceanic asthenosphere. *Earth and Planetary Science Letters*, 484, 204-212.

898 GIRARD, J., CHEN, J., RATERRON, P. & HOLYOKE, C. W., III 2013. Hydrolytic weakening of  
899 olivine at mantle pressure: Evidence of 100 (010) slip system softening from single-  
900 crystal deformation experiments. *Physics of the Earth and Planetary Interiors*, 216,  
901 12-20.

902 GRANT, K. J., KOHN, S. C. & BROOKER, R. A. 2006. Solubility and partitioning of water in  
903 synthetic forsterite and enstatite in the system  $\text{MgO-SiO}_2\text{-H}_2\text{O} \pm \text{Al}_2\text{O}_3$ .  
904 *Contributions to Mineralogy and Petrology*, 151, 651-664.

905 GREEN, D. H. & RINGWOOD, A. E. 1970. Mineralogy of peridotitic compositions under upper  
906 mantle conditions. *Physics of the Earth and Planetary Interiors*, 3, 359-371.

907 HERMANN, J., O'NEILL, H. S. C. & BERRY, A. J. 2005. Titanium solubility in olivine in the  
908 system  $\text{TiO}_2\text{-MgO-SiO}_2$ : no evidence for an ultra-deep origin of Ti-bearing olivine.  
909 *Contributions to Mineralogy and Petrology*, 148, 746-760.

910 JACOBSEN, S. D., JIANG, F., MAO, Z., DUFFY, T. S., SMYTH, J. R., HOLL, C. M. & FROST, D. J.  
911 2008. Effects of hydration on the elastic properties of olivine. *Geophysical Research*  
912 *Letters*, 35.

913 JOLLANDS, M. C., O'NEILL, H. S., BERRY, A. J., LE LOSQ, C., RIVARD, C. & HERMANN, J. 2021. A  
914 combined Fourier transform infrared and Cr K-edge X-ray absorption near-edge  
915 structure spectroscopy study of the substitution and diffusion of H in Cr-doped  
916 forsterite. *European Journal of Mineralogy*, 33, 113-138.

917 JUNG, H. & KARATO, S. 2001. Water-induced fabric transitions in olivine. *Science*, 293, 1460-  
918 1463.

919 KARATO, S., JUNG, H., KATAYAMA, I. & SKEMER, P. 2008. Geodynamic significance of seismic  
920 anisotropy of the upper mantle: New insights from laboratory studies. *Annual*  
921 *Review of Earth and Planetary Sciences*.

922 KARATO, S. I. & JUNG, H. 2003. Effects of pressure on high-temperature dislocation creep in  
923 olivine. *Philosophical Magazine*, 83, 401-414.

924 KARATO, S. I., PATERSON, M. S. & FITZ GERALD, J. D. 1986. RHEOLOGY OF SYNTHETIC  
925 OLIVINE AGGREGATES - INFLUENCE OF GRAIN-SIZE AND WATER. *Journal of*  
926 *Geophysical Research-Solid Earth and Planets*, 91, 8151-8176.

927 KENT, A. J. R. & ROSSMAN, G. R. 2002. Hydrogen, lithium, and boron in mantle-derived  
928 olivine: The role of coupled substitutions. *American Mineralogist*, 87, 1432-1436.

929 KOHLSTEDT, D. L. 2006. The role of water in high-temperature rock deformation. In:  
930 KEPLER, H. & SMYTH, J. R. (eds.) *Water in Nominally Anhydrous Minerals*. Chantilly:  
931 Mineralogical Soc Amer & Geochemical Soc.

932 KOHLSTEDT, D. L., KEPLER, H. & RUBIE, D. C. 1996. Solubility of water in the alpha, beta and  
933 gamma phases of  $(\text{Mg,Fe})_2\text{SiO}_4$ . *Contributions to Mineralogy and Petrology*, 123,  
934 345-357.

935 KUDOH, Y., KURIBAYASHI, T., KAGI, H. & INOUE, T. 2006. Cation vacancy and possible  
936 hydrogen positions in hydrous forsterite,  $\text{Mg}_{1.985}\text{Si}_{0.993}\text{H}_{0.06}\text{O}_4$ , synthesized at  
937 13.5 GPa and 1300 degrees C. *Journal of Mineralogical and Petrological Sciences*,  
938 101, 265-269.

939 LE LOSQ, C., JOLLANDS, M. C., TOLLAN, P. M. E., HAWKINS, R. & O'NEILL, H. S. C. 2019. Point  
940 defect populations of forsterite revealed by two-stage metastable hydroxylation  
941 experiments. *Contributions to Mineralogy and Petrology*, 174.

942 LEMAIRE, C., KOHN, S. C. & BROOKER, R. A. 2004. The effect of silica activity on the  
943 incorporation mechanisms of water in synthetic forsterite: a polarised infrared  
944 spectroscopic study. *Contributions to Mineralogy and Petrology*, 147, 48-57.

945 LU, R. & KEPLER, H. 1997. Water solubility in pyrope to 100 kbar. *Contributions to*  
946 *Mineralogy and Petrology*, 129, 35-42.

947 MACKWELL, S. J., KOHLSTEDT, D. L. & PATERSON, M. S. 1985. THE ROLE OF WATER IN THE  
 948 DEFORMATION OF OLIVINE SINGLE-CRYSTALS. *Journal of Geophysical Research-Solid*  
 949 *Earth and Planets*, 90, 1319-1333.

950 MAO, Z., JACOBSEN, S. D., JIANG, F., SMYTH, J. R., HOLL, C. M., FROST, D. J. & DUFFY, T. S.  
 951 2010. Velocity crossover between hydrous and anhydrous forsterite at high  
 952 pressures. *Earth and Planetary Science Letters*, 293, 250-258.

953 MATVEEV, S., O'NEILL, H. S., BALLHAUS, C., TAYLOR, W. R. & GREEN, D. H. 2001. Effect of  
 954 silica activity on OH-IR spectra of olivine: Implications for low-aSiO<sub>2</sub> mantle  
 955 metasomatism. *Journal of Petrology*, 42, 721-729.

956 MEI, S. & KOHLSTEDT, D. L. 2000a. Influence of water on plastic deformation of olivine  
 957 aggregates 1. Diffusion creep regime. *Journal of Geophysical Research-Solid Earth*,  
 958 105, 21457-21469.

959 MEI, S. & KOHLSTEDT, D. L. 2000b. Influence of water on plastic deformation of olivine  
 960 aggregates 2. Dislocation creep regime. *Journal of Geophysical Research-Solid Earth*,  
 961 105, 21471-21481.

962 MIERDEL, K. & KEPPLER, H. 2004. The temperature dependence of water solubility in  
 963 enstatite. *Contributions to Mineralogy and Petrology*, 148, 305-311.

964 MOSENFELDER, J. L., DELIGNE, N. I., ASIMOW, P. D. & ROSSMAN, G. R. 2006. Hydrogen  
 965 incorporation in olivine from 2-12 GPa. *American Mineralogist*, 91, 285-294.

966 MOSENFELDER, J. L., LE VOYER, M., ROSSMAN, G. R., GUAN, Y., BELL, D. R., ASIMOW, P. D. &  
 967 EILER, J. M. 2011. Analysis of hydrogen in olivine by SIMS: Evaluation of standards  
 968 and protocol. *American Mineralogist*, 96, 1725-1741.

969 MUIR, J. M. R., JOLLANDS, M., ZHANG, F. W. & WALKER, A. M. 2020. Explaining the  
 970 dependence of M-site diffusion in forsterite on silica activity: a density functional  
 971 theory approach. *Physics and Chemistry of Minerals*, 47.

972 PADRON-NAVARTA, J. A. & HERMANN, J. 2017. A Subsolidus Olivine Water Solubility  
 973 Equation for the Earth's Upper Mantle. *Journal of Geophysical Research-Solid Earth*,  
 974 122, 9862-9880.

975 PADRON-NAVARTA, J. A., HERMANN, J. & O'NEILL, H. S. C. 2014. Site-specific hydrogen  
 976 diffusion rates in forsterite. *Earth and Planetary Science Letters*, 392, 100-112.

977 QIN, T., WENTZCOVITCH, R. M., UMEMOTO, K., HIRSCHMANN, M. M. & KOHLSTEDT, D. L.  
 978 2018. Ab initio study of water speciation in forsterite: Importance of the entropic  
 979 effect. *American Mineralogist*, 103, 692-699.

980 RAUCH, M. & KEPPLER, H. 2002. Water solubility in orthopyroxene. *Contributions to*  
 981 *Mineralogy and Petrology*, 143, 525-536.

982 SMYTH, J. R., FROST, D. J., NESTOLA, F., HOLL, C. M. & BROMILEY, G. 2006. Olivine hydration  
 983 in the deep upper mantle: Effects of temperature and silica activity. *Geophysical*  
 984 *Research Letters*, 33.

985 STOCKER, R. L. & SMYTH, D. M. 1978. EFFECT OF ENSTATITE ACTIVITY AND OXYGEN PARTIAL-  
 986 PRESSURE ON POINT-DEFECT CHEMISTRY OF OLIVINE. *Physics of the Earth and*  
 987 *Planetary Interiors*, 16, 145-156.

988 SUN, W., YOSHINO, T., KURODA, M., SAKAMOTO, N. & YURIMOTO, H. 2019. H-D  
 989 Interdiffusion in Single-Crystal Olivine: Implications for Electrical Conductivity in the  
 990 Upper Mantle. *Journal of Geophysical Research-Solid Earth*, 124, 5696-5707.

991 TOLLAN, P. M. E., O'NEILL, H. S. C. & HERMANN, J. 2018. The role of trace elements in  
 992 controlling H incorporation in San Carlos olivine. *Contributions to Mineralogy and*  
 993 *Petrology*, 173.

994 TOLLAN, P. M. E., SMITH, R., O'NEILL, H. S. C. & HERMANN, J. 2017. The responses of the  
 995 four main substitution mechanisms of H in olivine to H<sub>2</sub>O activity at 1050 degrees C  
 996 and 3 GPa. *Progress in Earth and Planetary Science*, 4.

- 997 UEKI, K., KUWATANI, T., OKAMOTO, A., AKAHO, S. & IWAMORI, H. 2020. Thermodynamic  
998 modeling of hydrous-melt-olivine equilibrium using exhaustive variable selection.  
999 *Physics of the Earth and Planetary Interiors*, 300.
- 1000 WALKER, A. M., HERMANN, J., BERRY, A. J. & O'NEILL, H. S. 2007. Three water sites in upper  
1001 mantle olivine and the role of titanium in the water weakening mechanism. *Journal*  
1002 *of Geophysical Research-Solid Earth*, 112, 12.
- 1003 WANG, D., MOOKHERJEE, M., XU, Y. & KARATO, S.-I. 2006. The effect of water on the  
1004 electrical conductivity of olivine. *Nature*, 443, 977-980.
- 1005 WITHERS, A. C. & HIRSCHMANN, M. M. 2007. H<sub>2</sub>O storage capacity of MgSiO<sub>3</sub> clinoenstatite  
1006 at 8-13 GPa, 1,100-1,400 degrees C. *Contributions to Mineralogy and Petrology*, 154,  
1007 663-674.
- 1008 WITHERS, A. C. & HIRSCHMANN, M. M. 2008. Influence of temperature, composition, silica  
1009 activity and oxygen fugacity on the H<sub>2</sub>O storage capacity of olivine at 8 GPa.  
1010 *Contributions to Mineralogy and Petrology*, 156, 595-605.
- 1011 WITHERS, A. C., HIRSCHMANN, M. M. & TENNER, T. J. 2011. The effect of Fe on olivine H<sub>2</sub>O  
1012 storage capacity: Consequences for H<sub>2</sub>O in the martian mantle. *American*  
1013 *Mineralogist*, 96, 1039-1053.
- 1014 XUE, X., KANZAKI, M., TURNER, D. & LOROCH, D. 2017. Hydrogen incorporation mechanisms  
1015 in forsterite: New insights from H-1 and Si-29 NMR spectroscopy and first-principles  
1016 calculation. *American Mineralogist*, 102, 519-536.
- 1017 ZHANG, B.-H. & XIA, Q.-K. 2021. Influence of water on the physical properties of olivine,  
1018 wadsleyite, and ringwoodite. *European Journal of Mineralogy*, 33, 39-75.

1019

1020

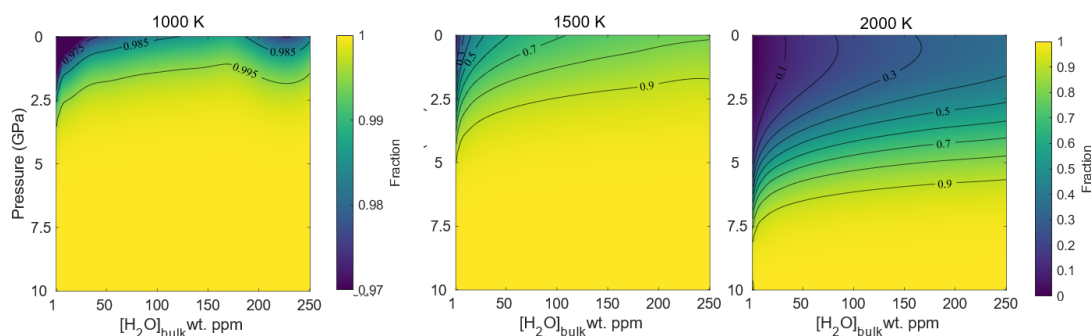


Figure 1: The fraction of  $\text{H}_2\text{O}_{\text{bulk}}$  that is in  $(4\text{H})_{\text{Si}}^{\times}$  ( $1 = \text{all water is } (4\text{H})_{\text{Si}}^{\times}$ ) as a function of  $[\text{H}_2\text{O}]_{\text{bulk}}$  and pressure at different temperatures for pure forsterite. The rest of the water ( $1-x$ ) is  $(2\text{H})_{\text{Mg}}^{\times}$  except for an extremely small amount ( $<0.001$  and generally much smaller) of water that exists as  $\text{H}_i^{\bullet}$  (Figure S1). Note that at 1000 K a different scale is used because the fraction of  $(4\text{H})_{\text{Si}}^{\times}$  does not go below 0.97 in these conditions. All other extrinsic and intrinsic defects have much lower concentrations ( $<1 \times 10^{-10}$  wt. ppm) in all cases. An alternative rendering against pressure and temperature with fixed  $[\text{H}_2\text{O}]_{\text{bulk}}$  is given in Figure S2. Data used to construct Fig 1, 2, 3, 5 and 6 is included in the supplementary spreadsheet.



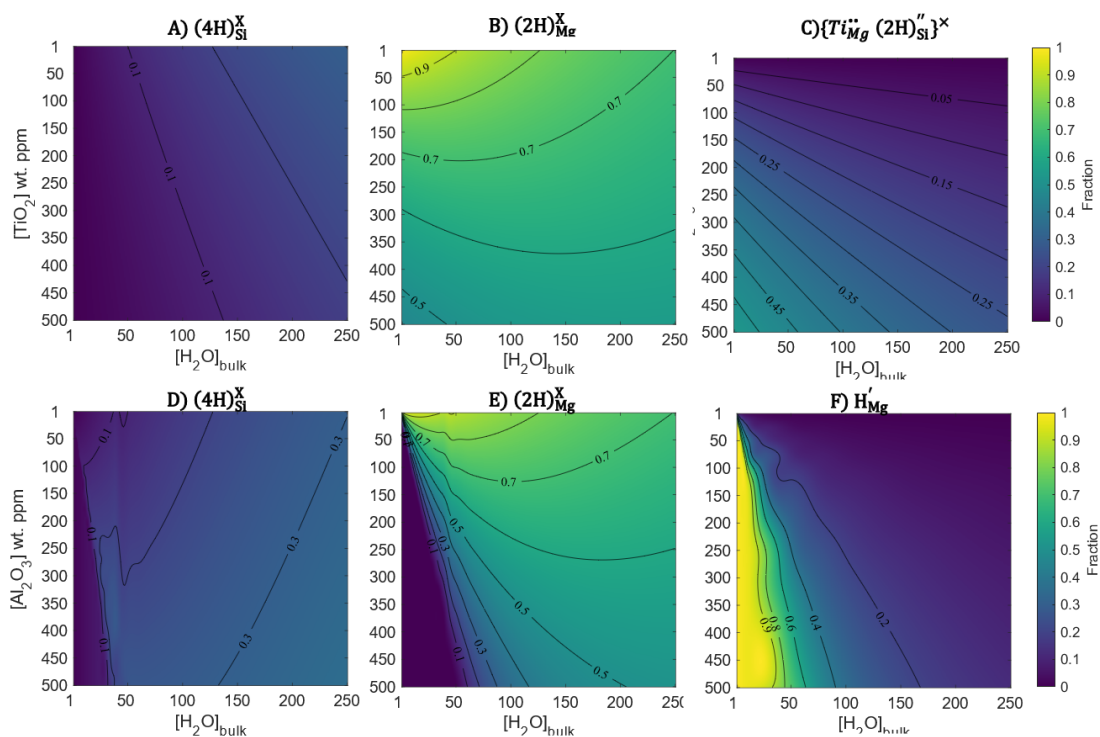


Figure 2: Plot of the fraction of  $\text{H}_2\text{O}_{\text{bulk}}$  that is in each defect (1= all water is in that defect) for each major H-bearing defects in forsterite as a function of  $[\text{H}_2\text{O}]_{\text{bulk}}$  and A-C)  $\text{TiO}_2$  (top row) and D-E)  $\text{Al}_2\text{O}_3$  at 2000 K and 0 GPa. Minor products are shown in Figure S4.

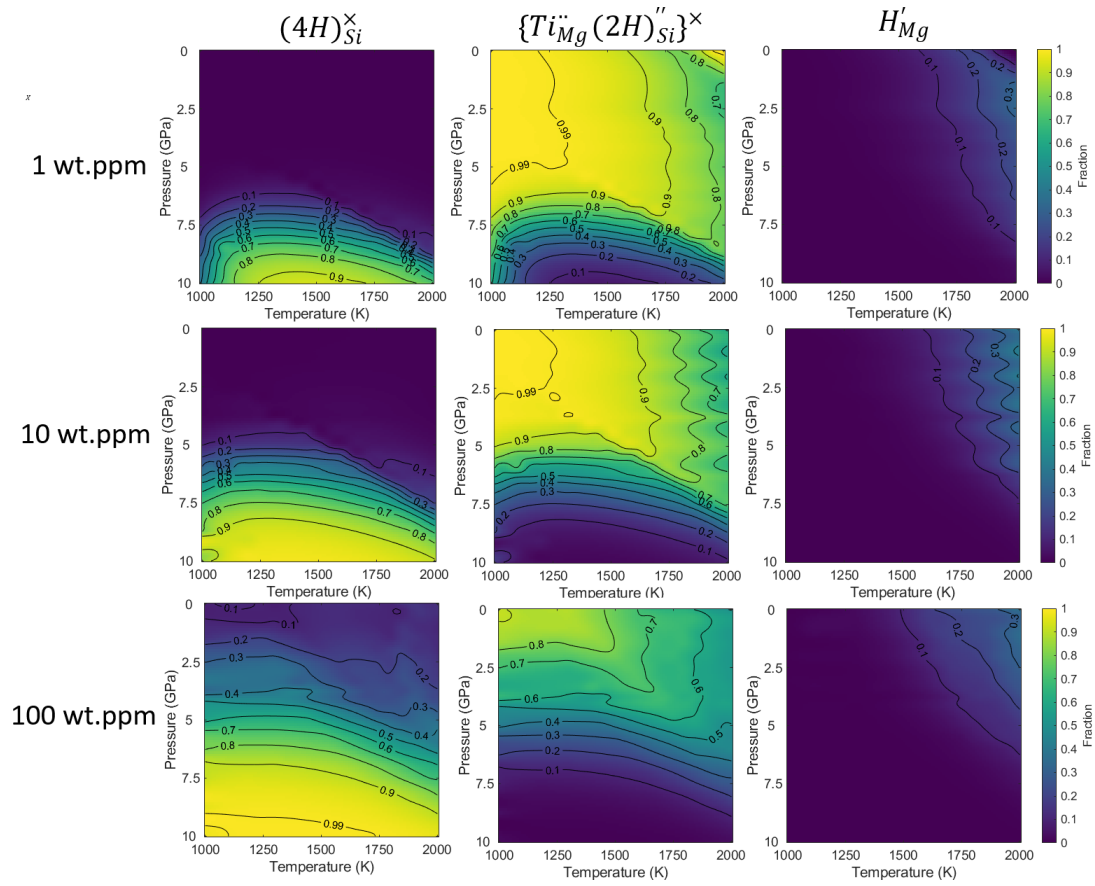


Figure 3: Plot of the fraction of  $\text{H}_2\text{O}_{\text{bulk}}$  that is in each defect (1= all water is in that defect) as a function of temperature and pressure with fixed total  $[\text{H}_2\text{O}]_{\text{bulk}}$  in forsterite containing 500 wt. ppm  $\text{Al}_2\text{O}_3$  and 500 wt. ppm  $\text{TiO}_2$  as a function of P and T. The three major defects are shown here, minor defects are shown in Figure S5. Due to the high amount of Al,  $\text{H}'_{\text{Mg}}$  is a major defect and  $(4\text{H})_{\text{Si}}^{\times}$  is a minor defect but with lower Al  $(2\text{H})_{\text{Mg}}^{\times}$  would become major and  $\text{H}'_{\text{Mg}}$  minor (see Figure 2) while the trends relative to  $(4\text{H})_{\text{Si}}^{\times}$  and  $\{\text{Ti}_{\text{Mg}}^{\bullet\bullet}(2\text{H})_{\text{Si}}^{\prime\prime}\}^{\times}$  would remain largely unchanged.

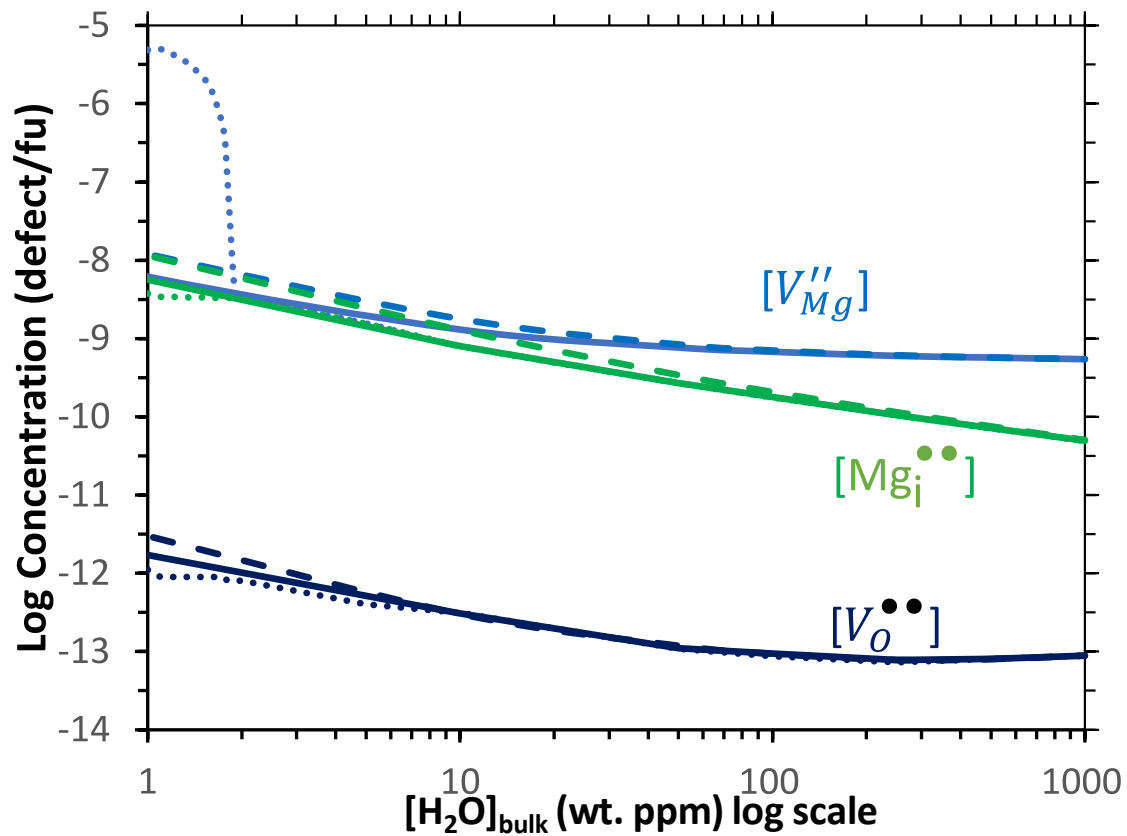
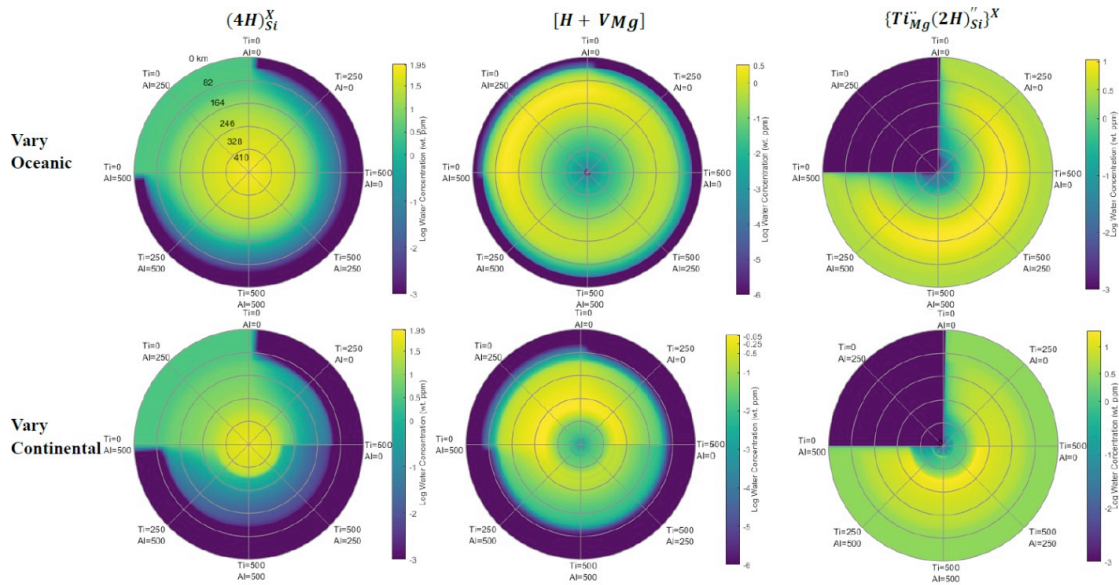


Figure 4: Plot of the three major intrinsic defects as a function of water concentration at 2000 K and 0 GPa (corrected) with three different crystal chemistries (solid line=pure forsterite, dashed line= 500 wt. ppm TiO<sub>2</sub>, dotted line= 500 wt. ppm Al<sub>2</sub>O<sub>3</sub>). The only major difference induced by crystal chemistry is Al induces extra  $V''_{Mg}$  due to R8 but this effect is suppressed by even low amounts water. The absolute value of these concentrations is less constrained than for extrinsic defects as their concentration is much smaller but relative trends with  $[H_2O]_{bulk}$  are better constrained.



1062

1063 Figure 5: Plot of  $\log_{10}$  of the concentration of water (ratio of water in each defect  
 1064 multiplied by  $[\text{H}_2\text{O}]_{\text{bulk}}$  in wt. ppm) in each of the three major defects:  $(4\text{H})_{\text{Si}}^{\times}$ , hydrated  
 1065 Mg sites  $(2\text{H})_{\text{Mg}}^{\times} + \text{H}_{\text{Mg}}'$ - labelled as  $[\text{H} + \text{VMg}]$ , and  $\{\text{Ti}_{\text{Mg}}^{\times}(2\text{H})_{\text{Si}}^{\prime\prime}\}^{\times}$ . This is along an  
 1066 oceanic or continental geotherm with water content varying with depth (Table S17)  
 1067 and with varying Ti and Al contents. From the top ( $\text{Al}_2\text{O}_3=0$  wt. ppm,  $\text{TiO}_2=0$  wt.  
 1068 ppm) going clockwise  $\text{TiO}_2$  concentration increases up to 90 degrees ( $\text{Al}_2\text{O}_3=0$  wt.  
 1069 ppm,  $\text{TiO}_2=500$  wt. ppm) then  $\text{Al}_2\text{O}_3$  up to 180 degrees ( $\text{Al}_2\text{O}_3=500$  wt. ppm,  $\text{TiO}_2=$   
 1070 500 wt. ppm) then  $\text{TiO}_2$  decreases up to 270 degrees ( $\text{Al}_2\text{O}_3=500$  wt. ppm,  $\text{TiO}_2=0$   
 1071 wt. ppm) before  $\text{Al}_2\text{O}_3$  decreases back to 0.  $[\text{H} + \text{VMg}]$  values have been truncated to -  
 1072 6,  $(4\text{H})_{\text{Si}}^{\times}$  and  $\{\text{Ti}_{\text{Mg}}^{\times}(2\text{H})_{\text{Si}}^{\prime\prime}\}^{\times}$  graphs to -3, in the truncated region there are often very  
 1073 sharp decreases in concentration until there is effectively none of that product. Data  
 1074 was calculated at a series of gridpoints (supplementary spreadsheet) that were then  
 1075 interpolated using the inter2p spline method of MATLAB. Very sharp changes are  
 1076 seen around the cardinal directions where concentration of one extrinsic atom (Ti or  
 1077 Al) goes to 0, this is because very large changes in H distribution occur over very  
 1078 small ranges of  $\text{Al}_2\text{O}_3$  or  $\text{TiO}_2$  when they are small. Such small concentrations are  
 1079 poorly visualised in this graph but probably are not important in the mantle.

1080

1081

1082

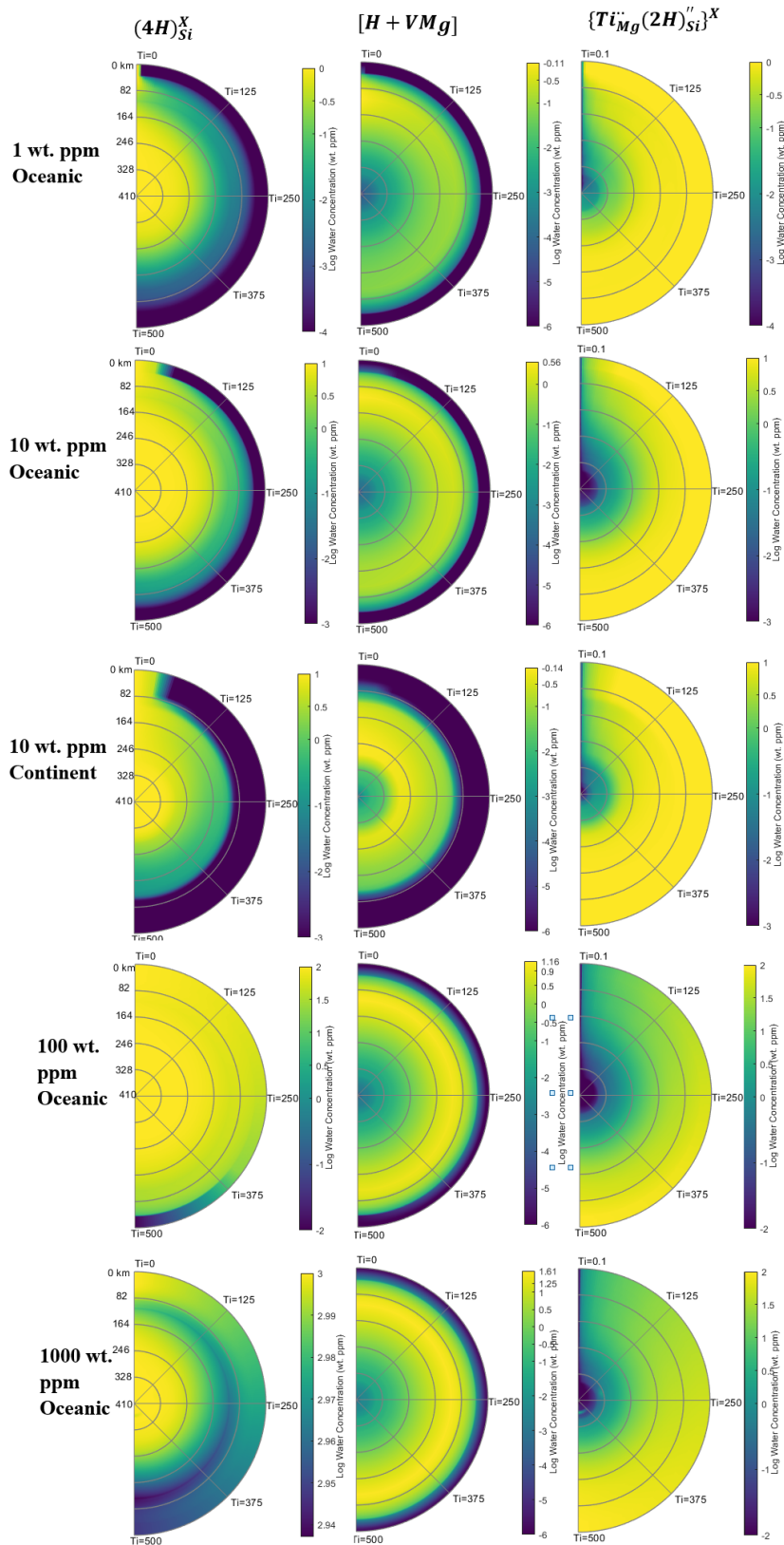


Figure 6: As Figure 5 but with fixed  $[H_2O]_{\text{bulk}}$  (given in wt. ppm) irrespective of depth. These graphs vary the concentration of  $TiO_2$  only going from  $TiO_2 = 0.1$  wt. ppm at 0 degrees to,  $TiO_2 = 500$  wt. ppm at 180 degrees with no  $Al_2O_3$  present.

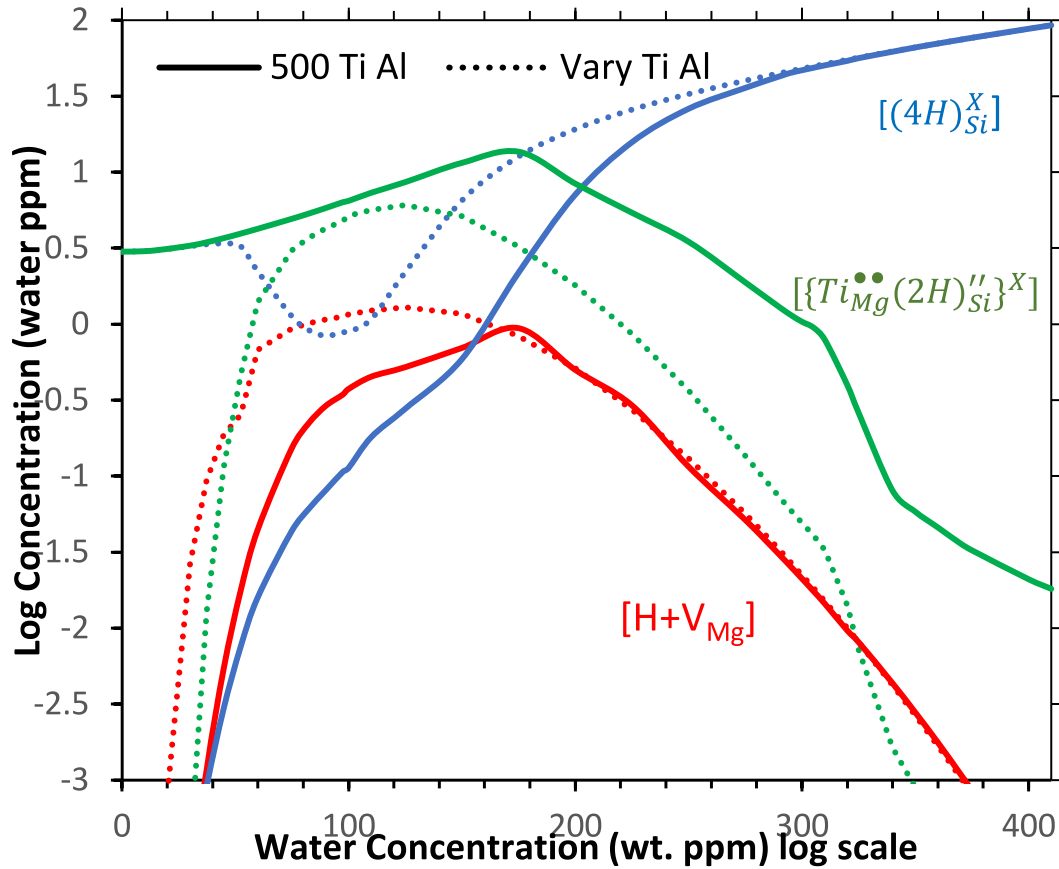


Figure 7: Plot of the concentration of the major H-bearing defects as a function of depth along an oceanic geotherm with varied water concentration with depth (Table S17). Solid lines represent a fixed  $\text{TiO}_2$  and  $\text{Al}_2\text{O}_3$  concentration of 500 wt. ppm, the dotted line represent a varied  $\text{TiO}_2$  and  $\text{Al}_2\text{O}_3$  concentration with depth (Table S17). The lines have significant roughness which is likely due to a lack of granularity in our water distribution and geotherm functions, with a fixed water concentration (Figure S6-S9) trends are smoother. The same graph along a continental geotherm is shown in Figure S6 and with varying fixed water concentrations along an oceanic geotherm in Figure S7-S9.

	0 GPa			5 GPa			10 GPa		
	1000 K	1500 K	2000 K	1000 K	1500 K	2000 K	1000 K	1500 K	2000 K
R1	-1.337	-1.336	-1.337	-2.139	-2.119	-1.794	-3.376	-3.672	-3.413
R2	0.585	0.585	0.585	0.564	0.564	0.565	0.564	0.564	0.565
R3	6.639	6.891	7.142	7.772	8.700	9.627	8.554	9.954	11.354
R4	-1.031	-1.045	-1.006	-1.169	-1.183	-1.150	-1.281	-1.296	-1.272
R5	-0.421	-0.282	0.021	-0.765	-0.585	-0.240	-1.071	-0.871	-0.513
R6	-1.948	-2.032	-2.147	-2.331	-2.452	-2.556	-2.525	-2.733	-2.881
R7	1.157	1.099	1.071	1.227	1.211	1.248	1.142	1.124	1.178
R8	-1.282	-1.175	-1.056	-1.706	-1.661	-1.591	-1.879	-1.910	-1.903
R9	4.278	4.223	4.207	4.464	4.440	4.537	4.472	4.388	4.490
R10	-4.551	-4.607	-4.640	-4.937	-5.042	-5.187	-4.907	-4.987	-5.163
R11	2.121	2.140	2.100	2.387	2.603	2.705	2.560	2.842	3.023
R12	-2.179	-2.166	-2.124	-2.814	-2.934	-2.994	-3.198	-3.480	-3.678
R13	-0.959	-0.949	-0.951	-1.296	-1.311	-1.311	-1.680	-1.747	-1.776
R24	0.270	0.282	0.298	0.239	0.254	0.269	0.231	0.258	0.278

1099 Table 1: Reaction energies (in eV/f.u) for the hydrated defect reactions (R1-R10) and  
1100 some other important reactions as a function of pressure and temperature. All other  
1101 reactions are shown in Table S12.

1102

1103

1104

			$[(2H)_{Mg}^{\times} + H'_{Mg}]$	$[(4H)_{Si}^{\times}]$	$[\{Ti_{Mg}^{\bullet\bullet}(2H)''_{Si}\}^{\times}]$	$[V''_{Mg}]$	$[Mg_i^{\bullet\bullet}]$	$[V_O^{\bullet\bullet}]$	$[V_{Si}^{\bullet\bullet}]_{proj}$	$rc \rightarrow rf$ ( $a_{rat}$ )
Pure	0 GPa	2000 K	0.82	1.63	n/a	-0.14	-0.84	-0.83	-0.29	1.03/ 1.18
		1500 K	0.60	1.19	n/a	-0.01	0.00	0.00	-0.01	1.34/ 1.78
		1000 K	0.50	1.01	n/a	-0.01	0.00	0.00	-0.01	1.95/ 1.98
	10 GPa	2000 K	0.50	1.00	n/a	-0.49	-0.49	0.00	-0.99	1.99/ 2.00
		1500 K	0.50	1.00	n/a	0.13	0.00	0.00	0.26	2.00/ 2.00
		1000 K	0.50	1.00	n/a	0.34	0.00	0.00	0.69	2.00/ 2.00
TiO <sub>2</sub> = 500 ppm Al <sub>2</sub> O <sub>3</sub> = 500 ppm	0 GPa	2000 K	1.22	2.79	0.51	-0.56	0.00	0.00	-1.30	0.97/ 0.98
		1500 K	1.29	2.86	0.49	-0.82	-0.80	0.00	-1.81	1.00/ 1.01
		1000 K	1.35	2.95	0.48	-1.40	-1.51	0.00	-3.06	1.00/ 1.09
	10 GPa	2000 K	0.74	1.14	0.55	-0.53	-0.50	-0.14	-0.82	1.44/ 1.77
		1500 K	0.63	1.02	0.57	-0.19	-0.13	0.00	-0.32	1.86/ 1.91
		1000 K	0.50	1.00	0.58	-0.02	0.00	0.00	-0.04	1.91/ 2.00

Table 2: The water exponent  $rc$  determined for each of these systems between 10-1000 wt. ppm water. The final column shows a conversion factor  $a_{rat}$  ( $a_{rat} * rc = rf$ ) for converting from  $rc$  into  $rf$  determined at  $[H_2O]_{bulk}$  10/100 wt. ppm. The fitting method and the mechanism for calculating the last column is presented in the supplementary information. The first column shows the combined  $rc$  for  $[(2H)_{Mg}^{\times} + H'_{Mg}]$ . For pure forsterite this is the exponent for  $(2H)_{Mg}^{\times}$  as  $H'_{Mg}$  is negligible. For the Al+Ti containing forsterite this is the exponent for  $H'_{Mg}$  as  $(2H)_{Mg}^{\times}$  is a minor product. An exponent for  $V_{Si}^{\bullet\bullet\bullet}$  cannot be reliably determined because it's concentration is small but its concentration is overwhelmingly controlled by R14 and thus its exponent should be roughly double that of  $V_{Mg}^{\bullet\bullet}$  similarly to how  $[HSi]$  is roughly twice  $[HMg]$  because it is controlled by R1.